THE UNIVERSITY OF QUEENSLAND

AUSTRALIA

Design, Construction & Characterisation of

A Versatile High Atom Number BEC Apparatus

Thomas Andrew Bell
BSc, University of Queensland, 2011

Under the supervision of
Dr. Mark Baker

A thesis submitted to the University of Queensland
in partial fulfilment of the degree of Bachelor of Science with Honours
School of Mathematics and Physics
June 2014

Typeset in LaTeX 2_ε.

The work presented in this Thesis is, to the best of my knowledge and belief original, except as acknowledged in the text, and has not been submitted either in whole or in part, for a degree at this or any other university.

Thomas Andrew Bell

Abstract

Bose Einstein Condensates represent a valuable experimental medium for the study and application of fundamental atomic science. Within tailored trapping potentials, many exotic quantum phenomena may be probed or exploited, including Feshbach resonances [1], atomic clock measurements [2], Bragg spectroscopy [3], and superfluidity [4]. While experimental condensates were first produced within magnetic traps, optical potentials are advantageous for interferometry, since they permit spin entangled sensitivity enhancement [5]. Exploiting the strengths of each distinct approach, hybrid methods were proposed for the rapid production of large condensates within optical potentials [6]. Following the work of [7], the present thesis aims to experimentally develop an optimised hybrid apparatus for the rapid production of condensates within optical potentials. Although condensates have not yet been produced, many preliminary trapping configurations have been demonstrated, representing substantial progress for the year available. We have successfully generated large *Magneto-Optical Traps* with 3×10^9 atoms, and *Compressed Magneto-Optical Traps* of 1.2×10^9 at temperatures of 32μK. Long lived *Magnetic Traps* with up to 3×10^8 atoms have been additionally formed. Transfer into the magnetic potential is however not yet optimised, with larger numbers expected once magnetic bias fields are employed to spatially overlap trap centres. Implementing a period of optical pumping should also increase loading into the magnetic potential. To form condensates it remains to firstly compress and evaporatively cool within the magnetic potential. An *Optical Dipole Trap* must then be overlapped and evaporative cooling continued to degeneracy.

Contents

List of Figures

List of Abbreviations

AOM ..... Acousto-Optical Modulator
BEC ..... Bose-Einstein Condensate
BNC ..... Bayonet Neill-Concelman
CCD ..... Charge-Coupled Device
CMOT ..... Compressed Magneto-Optical Trap
DPDT ..... Double Pole Double Throw
FET ..... Field-Effect Transistor
FORT ..... Far Off Resonance Trap
FS ..... Fine Structure
GPE ..... Gross-Pitaevskii Equation
HFS ..... Hyper-Fine Structure
HV ..... High Vacuum
LVIS ..... Low-Velocity Intense Source
MOSFET ... Metal-Oxide-Semiconductor Field-Effect Transistor
MOT ..... Magneto-Optical Trap
ODT ..... Optical Dipole Trap
OET ..... Optical Earnshaw Theorem
OM ..... Optical Molasses
PBS ..... Polarising Beam Splitter
PM ..... Polarisation Maintaining
RF ..... Radio Frequency
SAM ..... Spin Angular Momentum
SPDT ..... Single Pole Double Throw
SQ ..... Spherical Quadrupole
TAAP ..... Time-Averaged Adiabatic Potential
TOP ..... Time-Orbiting Potential
TTL ..... Transistor-Transistor Logic
UHV ..... Ultra-High Vacuum

1 Introduction

Bose Einstein Condensates (BEC) represent a valuable experimental medium for the study and application of fundamental atomic science. Within tailored trapping potentials, many exotic quantum phenomena may be probed or exploited, including Feshbach resonances [1], atomic clock measurements [2], Bragg spectroscopy [3], and superfluidity [4]. This exotic phase of matter manifests in dilute bosonic gas, when macroscopic quantities degenerately occupy the lowest energy state. Experimental production of BEC therefore requires methods for thermally isolating, confining and cooling a thermal source of atoms. For neutral atomic gases, conservative forces induced within applied electromagnetic fields are ideal. Finding the optimal combination of trapping potentials for the rapid & efficient production of large & sustainable condensates is however an ongoing task. While condensates were first produced within magnetic traps, optical potentials are advantageous for interferometry, since they permit spin entangled sensitivity enhancement [5]. Despite providing tighter confinement, the comparative difficulty of producing large BEC has limited the success of all-optical systems. To exploit the strengths of each distinct approach, hybrid methods were proposed for the rapid production of large BEC [6]. Following the demonstration in [7], the present thesis aims to experimentally develop an optimised hybrid apparatus for the rapid production of condensates within optical potentials.

1.1 Methodology

One of the many significant experimental milestones toward demonstrating BEC was the development of *Magneto-Optical Traps* (MOT) [8]. While condensates cannot be directly formed, greater loading into magnetic potentials may be achieved via MOT transfer than direct loading of a thermal vapour. Since evaporative cooling is necessary within conservative magnetic potentials, greater initial loading increases the cooling duration, thereby reducing the minimum achievable temperature. Obtaining sufficient atoms for sustained

evaporation to degeneracy was finally achieved in 1995, when BEC were first formed experimentally within magnetic potentials [9, 10]. While many further magnetic potentials have since been developed, including *Time Averaged Adiabatic Potentials* (TAAP) suitable for atomic interferometry [11], the confining interaction is spin dependant. *Far Off Resonance Traps* (FORT), a variety of *Optical Dipole Trap* (ODT), are alternatively spin independent, releasing the internal atomic degree of freedom. Within optical potentials interferometric measurement sensitivities may therefore be enhanced through spin entanglement [5], independent of the confining potential. Despite condensates forming more rapidly, ODT require prohibitively high laser powers for simultaneous depth and volume, producing typically two orders smaller BEC [12]. To increase the final atom number two stage regimes were proposed, where a larger shallower ODT would mediate increased loading into a second deeper ODT. However, since superlative optical alignment is required for high fidelity transfer between ODT, hybrid magnetic potentials were alternatively investigated to mediate the transition from MOT [6]. An important demonstration of this hybrid path in [7] represents the primary comparative reference for the method developed in this thesis (figure 1.1).

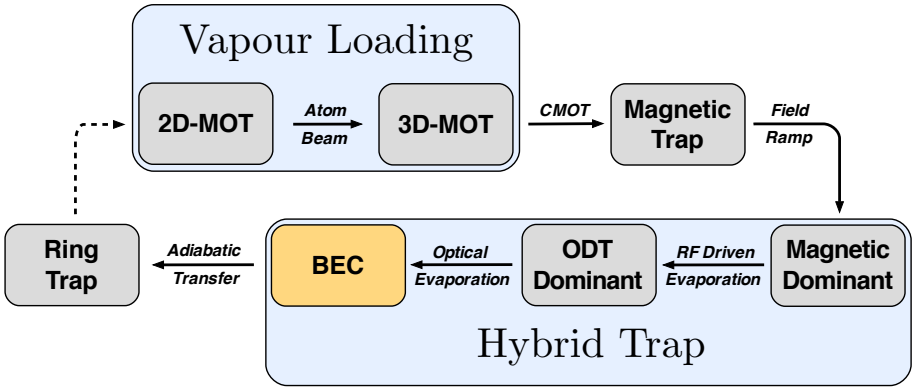

FIGURE 1.1: Summary schematic of hybrid condensation method. Distinct confinement stages are indicated within grey boxes, and the transition processes labeled in italics. As represented, both the initial vapour loading and hybrid trapping method encompass more than one process. Further details for each confinement stage and transition process are provided in chapter 2.

1.2 Thesis Overview

Between the present method of this thesis and the comparative paper [7], three critical differences are worth highlighting. Great effort has firstly gone into optimising the magnetic coil system, thereby reducing the electrical power required for equivalent magnetic field strength (section 3.4.1). Secondly, an alternative primary vapour loading method provides greater flexibility and substantially reduced the total size of the vacuum chamber (section 3.3). Finally, the system has been designed in order to be flexible in the variety of trapping potentials that can be produced. Although the primary motivation is to produce a system capable of generating stable ring trap geometries, with high atom number using a scanned optical dipole trap, additional features were incorporated for future applications. This includes the

construction of additional *Bias* & *RF* coils around the science cell, respectively implemented to facilitate TOP traps & RF dressed potentials (section 3.5.1). Note both potentials are mentioned here only for completeness and further details are outside the scope of this thesis.

Chapter 2 provides summary background information relevant for an understanding of experimental work presented in later chapters. Emphasis has been placed on consolidating different conceptual conventions used for describing relevant trapping potentials. Theoretical justification for BEC is firstly provided, and the necessary experimental conditions identified. Fundamental principles for each distinct electromagnetic potential within the present method are then individually addressed, providing justification for later design decisions.

Chapter 3 provides the major elements of design and construction undertaken toward the development of a new experimental setup. Representing the majority of work undertaken, this chapter is presented in rough chronological order.

Chapter 4 provides operational results for preliminary trapping potentials completed within one year. The data includes absorption images, atom numbers and cloud temperatures. Optimisation and measurement techniques are additionally described.

Chapter 5 provides a succinct summary of progress made, and outlines the future direction of the project toward condensate formation.

2 Theoretical Background

2.1 Bose-Einstein Condensation

When a dilute atomic vapour of neutral bosons is sufficiently cooled, macroscopic quantities may undergo a phase transition. Known as Bose-Einstein Condensation, collective wave behaviour manifests as the distinction between discrete particles becomes obscured. While any boson variety should exhibit this behaviour, only select elements possess suitable properties to practically enable adequate cooling and confinement. Fewer still demonstrate the necessary elastic scattering properties for stable condensation. Of greatest interest are single valence *Alkali Metals*, for which the comparatively simple common internal structure satisfies the first criteria. In particular, the mutually repulsive scattering properties of *Rubidium-87*, characterised by a positive scattering length, additionally satisfy the second criteria. Curiously, the original proliferation of ^{87}Rb was in part motivated by the increased availability of near resonant diode lasers, developed primarily for CD drives. Indeed our present use of ^{87}Rb is partially motivated by existing laboratory infrastructure. The primary objective of the following section is to substantiate this choice. Firstly, the physical conditions required for BEC within harmonic optical potentials are described. The ^{87}Rb internal energy structure, which facilitates electromagnetic confinement, is presented. This section then concludes with a discussion of inelastic collisional loss mechanisms, and outlines methods for mitigating such loss.

2.1.1 Fundamental Statistics

Depending on whether a particles total spin takes a full or half integer value, they are respectively categorised as bosonic or fermionic. While the Maxwell-Boltzman distribution adequately describes both particles for classical energies, on the quantum scale Bose-Einstein

and Fermi-Dirac statistics respectively emerge. Significant for the present work is the collective behaviour of low temperature Bosons within harmonic optical potentials, for which only discrete energies are permitted. For a given temperature, the occupation N_i for state i is the expected number of particles with the energy ϵ_i [13]. Given k_B is constant, the chemical potential μ must be extensive to account for the total particle number N.

$$N_i = \frac{1}{e^{(\epsilon_i-\mu)/k_BT}-1} \tag{2.1}$$

Given the occupation of individual states, one may derive an expression for N by summating over all non-trivially occupied energies. However, in the limit of high temperature and large N, where many terms contribute, one may reasonably treat the distribution of states continuously. In the integral form $g(\epsilon)$ represents the density of states.

$$N = \int_0^\infty \frac{g(\epsilon)d\epsilon}{e^{(\epsilon-\mu)/k_BT}-1} \tag{2.2}$$

For a three dimensional harmonic potential, $g(\epsilon)$ is defined using the geometric frequency $\bar{\omega}$, where $\omega_{x,y,z}$ are cartesian trap frequencies [12].

$$g(\epsilon) = \frac{\epsilon^2}{2\hbar^3\bar{\omega}^3} \quad : \quad \bar{\omega} = (\omega_x\omega_y\omega_z)^{1/3} \tag{2.3}$$

For decreasing temperature, where μ approaches the ground state energy $\epsilon_0 = 0$, equation 2.2 may be solved for the harmonic potential described by equation 2.3 [11]. Elucidated in this process is the existence of a critical temperature T_C, below which the ground state occupation N_0 may become macroscopically large. Constituting a distinct phase, the degenerate ground state atoms represent a Bose-Einstein Condensate.

$$\frac{N_0}{N} = 1 - \left(\frac{T}{T_C}\right)^3 \quad : \quad T_C = 0.94\left(\frac{\hbar\bar{\omega}}{k_B}\right)N^{1/3} \tag{2.4}$$

While justifying the existence and heralding the onset of BEC, the present treatment does little to describe the ultimate dynamics of degenerate gases. For completeness I merely state that a thorough treatment would require solutions for the *Gross-Pitaevskii Equation (GPE)* [14]. Furthermore, the expression for T_C in equation 2.3 is specific to harmonic potentials, and is experimentally dependant on trap frequencies. Consequently, the critical temperature does not represent a practical target for the onset of degeneracy. Instead the critical phase space density $\rho_C = 2.612$ is independent of trap type and strength [15]. Here n represents the number density, m the atomic mass, and Λ the temperature dependant DeBroglie wavelength. From equation 2.5 condensation may be additionally understood as Λ thermally expanding to exceed the interatomic separation, thereby obscuring the distinction of individual particles.

$$\rho = n\Lambda^3 \qquad \Lambda = \left(\frac{2\pi\hbar^2}{mk_BT}\right)^{1/2} \tag{2.5}$$

2.1.2 Rubidium-87

To first approximation, the discrete bound states of atomic electrons are uniquely defined by a principle, azimuthal, and magnetic quantum number $|n, l, m_L\rangle$ [16]. However this model treats only the electron orbital angular momentum $\mathbf{L}$, neglecting spin angular momentum intrinsic to both the electron $\mathbf{S}$ and nucleus $\mathbf{I}$. Summating the electron spin and orbital momenta distinguishes the *Fine Structure* with total electron angular momenta $\mathbf{J} = \mathbf{L} + \mathbf{S}$. Further addition of the nuclear spin distinguishes the *Hyperfine Structure* with total atomic angular momenta $\mathbf{F} = \mathbf{J} + \mathbf{I}$ [17]. Analogous to the gross structure model, the magnitude of fine and hyperfine state momenta are identified with azimuthal quantum numbers j & f respectively. Integers m_J & m_F additionally identify the $2j+1$ and $2f+1$ substates ascribed by spin multiplicity.

$$\begin{aligned} \mathbf{L}^2|l, m_L\rangle &= \hbar^2 l\,(l+1)\,|l, m_L\rangle \\ \mathbf{L}_\mathrm{z}|l, m_L\rangle &= \hbar m_L|l, m_L\rangle \end{aligned} \tag{2.6}$$

$$\begin{aligned} \mathbf{J}^2|j, m_J\rangle &= \hbar^2 j\,(j+1)\,|j, m_J\rangle & \mathbf{F}^2|f, m_F\rangle &= \hbar^2 f\,(f+1)\,|f, m_F\rangle \\ \mathbf{J}_\mathrm{z}|j, m_J\rangle &= \hbar m_J|j, m_J\rangle & \mathbf{F}_\mathrm{z}|f, m_F\rangle &= \hbar m_F|f, m_F\rangle \end{aligned}$$

While free space degenerate, substates may experience inhomogeneous energy shifts within applied electromagnetic fields. Homogeneous confinement within spin dependant potentials therefore requires the alignment of atomic moments. *Spin Polarisation* describes such an alignment, whereby the sample majority occupy one substate. This condition may be achieved practically within *Optical Molasses*, by exploiting the Spin Angular Momenta (SAM) carried by circular polarised optical beams [18]. Through repeated spontaneous emission with dissimilar optical polarisation, atoms accumulate SAM parallel the beam axis [19]. Atoms are thus optically pumped to a substate with maximal amplitude.

$$\begin{aligned} \Delta m_F &= 0 \quad (\pi \text{ photon}) \\ \Delta m_F &= \pm 1 \quad (\sigma^{\pm} \text{ photon}) \end{aligned} \tag{2.7}$$

Spin polarisation additionally facilitates closed cycle optical cooling. Closed transition cycles minimise the number of laser frequencies required for sustained interaction. Given the minimal structure of monovalent alkali metals, many isotopes with suitable structure have been identified. For ^{87}Rb the hyperfine transition of interest is represented in figure 2.1a. This cycle is considered stable, since electric dipole selection rules forbid spontaneous decay to other states [20].

$$\begin{aligned} \Delta n &\rightarrow \text{unrestricted} \\ \Delta l &= \pm 1 \\ \Delta s &= 0 \\ \Delta j &= 0,\ \pm 1 \quad (j = 0 \nrightarrow 0) \end{aligned} \tag{2.8}$$

The dominate loss mechanism is instead non-resonant stimulation of the $|5\mathrm{S}_{1/2}, f = 2\rangle \rightarrow |5\mathrm{P}_{3/2}, f = 2\rangle$ transition, permitting subsequent decay into the lower $|5\mathrm{S}_{1/2}, f = 1\rangle$ ground state [21]. Since the 6.8GHz hyperfine ground splitting well exceeds the 6MHz natural line width of the cooling transition, these atoms no longer interact [22]. A secondary repump frequency is thus required to return lost atoms to the cooling cycle (figure 2.1b).

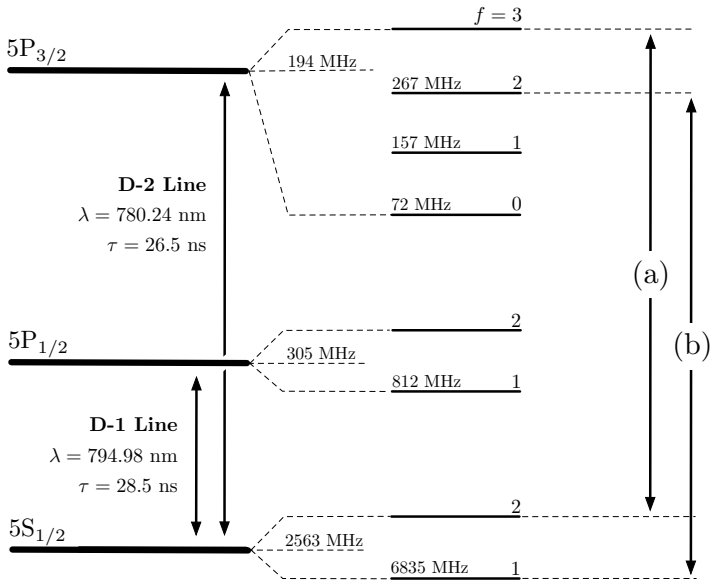

FIGURE 2.1: Hyperfine energy structure for ^{87}Rb and the transitions exploited for optical confinement [17]. (a) Primary cooling transition used in optical molasses and magneto-optical traps. For both processes the laser frequency is red-detuned by 15MHz. (b) Repump transition required to recycle atoms lost from the cooling cycle to the lower ground state through non-resonant or scattering interactions. Unlike the cooling light, the repump laser is locked on resonance.

2.1.3 Trap Number

While rapid & efficiency production is optimal, the size & stability of replicable condensates ultimately determines the quality of the generating procedure. Quantitative analysis and responsive design therefore require an understanding of particle growth and loss mechanisms. Hence the following section considers, in summary, each contribution to the rate equation 2.9, which models the confined particle number N with density distribution $n(\mathbf{r}, t)$ [23, 24]. Firstly consider the single growth term δ, which describes initial loading of thermal vapour into MOT. Either via direct background loading at uniform pressure, or the atom beam method used in this thesis, growth is suitably independent of N.

$$\frac{dN}{dt} = \delta - \alpha N - \beta \int_V n^2(\mathbf{r}, t) d^3r - \gamma \int_V n^3(\mathbf{r}, t) d^3r \tag{2.9}$$

Later terms alternatively represent three orders of many-body loss, where higher order terms may reasonably be neglected. *Single-Body* background collisional losses (α) contribute most prominently, necessitating *Ultra-High Vacuum* (UHV) conditions and preventing continuous loading ($\delta \to 0$). As previously noted, loading atoms to facilitate sufficient evaporative cooling was one historical challenge in observing BEC. Maintaining UHV conditions also motivates the atom beam MOT loading procedure outlined in section 2.3.4. *Two-Body* losses (β) are next most dominant, describing spin flip collisions, light assisted binary collisions and

photo association [25]. The former example importantly motivates conservative confinement in the $|f = 1\rangle$ ground state, since despite being more weakly confined, the $|f = 2\rangle$ state suffers greater many-body loss. Similar arguments additionally justify the use of ^{87}Rb over ^{85}Rb, since the negative scattering length for the later promotes inelastic collisions. Finally the *Three-Body* loss rate γ is typically negligible except at high densities, or as $T \to T_C$, near condensation. This process involves two particles forming a bound dimer, boosting a third particle and resulting in the loss of all three. Beyond selecting inherently favourable isotopes, within optical potentials magnetic bias fields may additionally tune Feshbach resonances, further reducing many-body loss.

2.2 Magnetic Confinement

Interest in magnetic trapping potentials extends back before 1951, when hexapole fields within toroidal current arrangements were theoretically considered [26]. Given the capacity for enhanced spectroscopy, methods for efficiently driving evaporative cooling with applied radio-frequencies were proposed thereafter [27]. Stable magnetic confinement was not however experimentally demonstrated until 1985, when sodium vapour was successfully held within a *Magnetic Spherical Quadrupole* [28]. While interest in the production of BEC subsequently grew, early progress was hindered by three-body & *Majorana* loss, respectively encountered at high density & zero-field minima [29]. For the later, many alternative potentials with non-zero minima were developed, finally facilitating experimental BEC in 1995 [9, 10, 30]. In this section the physical interaction mediating magnetic confinement, known as the *Zeeman Effect*, will be firstly discussed. This knowledge will then be used to address the spherical quadrupole potential. Conditions for efficient evaporative cooling will then be summarised, followed by a brief discussion of Majorana loss and immune trapping potentials.

2.2.1 Zeeman Effect

In the presence of an external magnetic field the degeneracy of hyperfine atomic substates will be lifted. This non-uniform interaction between magnetic fields and atomic magnetic moments is known as the *Zeeman Effect* [31]. For suitably weak fields the induced energy shifts are described by hamiltonian $\mathcal{H}_B$, where $\boldsymbol{\mu}_F$ represents the hyperfine magnetic moments.

$$\mathcal{H}_B = -\boldsymbol{\mu}_F \cdot \mathbf{B} \tag{2.10}$$

Since $\boldsymbol{\mu}_F$ is a compound quantity however, defined through coupling of the total electron ($\boldsymbol{\mu}_J$) and nuclear ($\boldsymbol{\mu}_I$) moments, each will independently couple to the applied field. Hence for some suitably large field the independent external coupling must eventually exceed the internal interaction, at which point equation 2.10 makes little sense. Instead the internal coupling is more appropriately treated as a perturbation to the interaction of the field with independent moments.

$$\mathcal{H}'_B = -(\boldsymbol{\mu}_J + \boldsymbol{\mu}_I) \cdot \mathbf{B}' \tag{2.11}$$

For many practical purposes it is fortunately sufficient to perturbatively treat either $\mathcal{H}_B$ or $\mathcal{H}'_B$ by selecting the appropriate corresponding free space hamiltonian $\mathcal{H}_0$. In the weak and strong field case respectively, this approach derives the *Anomalous Zeeman* and *Paschen-Bach* effects, as they are historically known. Analytic treatment of intermediate field strengths is however in general prohibitively difficult. Instead numeric techniques are necessary to diagonalise the full hamiltonian [17]. For states with spherically symmetric charge distributions however, the *Breit-Rabi* solution may be analytically derived [22, 32]. Since the ^{87}Rb ground states have spherical symmetry, the analytic solutions are illustrated in figure 2.2, where E_{hfs} represents the zero field hyperfine ground state energy separation. From this picture, two points will be of later significance. Firstly, since the energy difference between levels is field dependant, the resonant frequency of atoms through non-uniform fields may be spatially dependant. Secondly, the Zeeman interaction constitutes a conservative potential which, for select states, may impart restoring force $\mathbf{F}$.

$$\mathbf{F}(\mathbf{B}) \;=\; -\nabla\mathcal{H}_B \tag{2.12}$$

While the force magnitude is field gradient dependant, the magnetic quantum number m_F determines the direction. Each state may therefore be classified as either *High* or *Low-Field Seeking*. Since field minima but not maxima may be generated in current-free space, only low field seeking states may be magnetically confined [33]. Hence of the eight hyperfine magnetic states, only $|f, m_F\rangle = |1,-1\rangle, |2,1\rangle, |2,2\rangle$ are magnetically trappable.

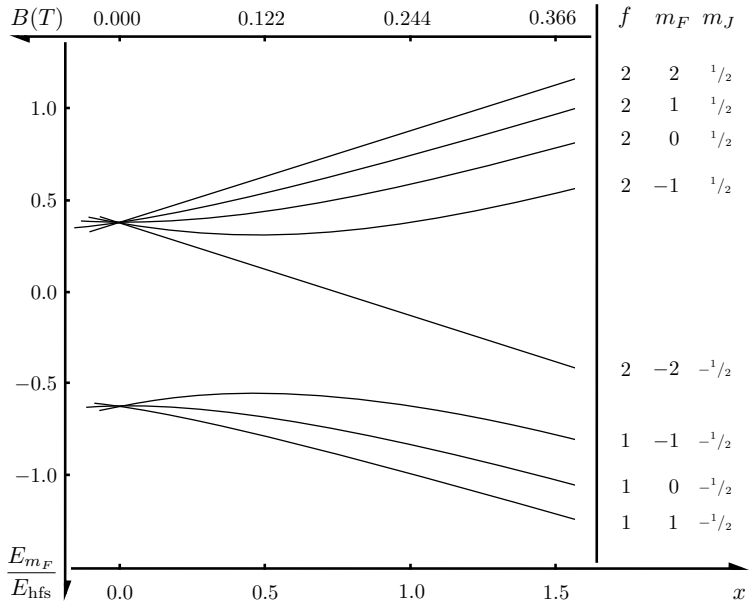

FIGURE 2.2: Breit-Rabi solutions for the ^{87}Rb hyperfine ground state Zeeman shifts. The magnetically induced energy shifts represented here importantly facilitate stable Magneto-Optical and pure Magnetic confinement. For the later, only low-field seeking states whose energy increases with field strength are magnetically trappable. Since $|f = 2, m_F = 2\rangle$ experiences the greatest increase it facilitates the strongest confinement. However $|1,-1\rangle$ is frequently used instead due to favourable scattering properties.

2.2.2 Spherical Quadrupole

Consisting of two circular anti-helmholtz configured current loops, the spherical quadrupole is the simplest magnetic potential to physically construct and mathematically model. Most significantly the central field is essentially linear, therefore imparting near spatially invariant restoring forces. Since the longitudinal gradient, represented along the z-axis, is twice that in the radial direction, it is most naturally aligned vertically to oppose gravity. Correspondingly, the quadrupole field $\mathbf{B}_{\mathrm{SQ}}$ is here expressed in terms of b, the gradient in the z-direction.

$$\mathbf{B}_{\mathrm{SQ}} = b\left(\frac{x}{2}\hat{\mathbf{e}}_x + \frac{y}{2}\hat{\mathbf{e}}_y + z\hat{\mathbf{e}}_z\right) \tag{2.13}$$

When substates are degenerate they are essentially indistinct. Only when the degeneracy is lifted within an applied field are they physically meaningful. Thus it is the local direction of the applied field which defines the quantisation axis, against which the substate of each atom is defined. To appreciate the significance of locality consider figure 2.3a. In this figure eight round particles are represented, with arrows indicating the direction of magnetic moments $\boldsymbol{\mu}_F$. Notice that while the magnetic moments are uniquely aligned relative the coordinate axis, all are similarly aligned relative the local field cross-section. Hence all the particles occupy the same state, and the sample may therefore be described as spin polarised. Also note, in the absence of inelastic spin change collisions, as atoms move adiabatically through the continuous field the local alignment of the magnetic moment is conserved. The essential features of stable magnetic confinement are therefore minimal inelastic interaction, and homogenous polarisation in a suitably low field seeking state. For the present work magnetic confinement is performed in the $|f = 1, m_F = -1\rangle$ state, since as mentioned previously, the two-body loss rate is substantially smaller.

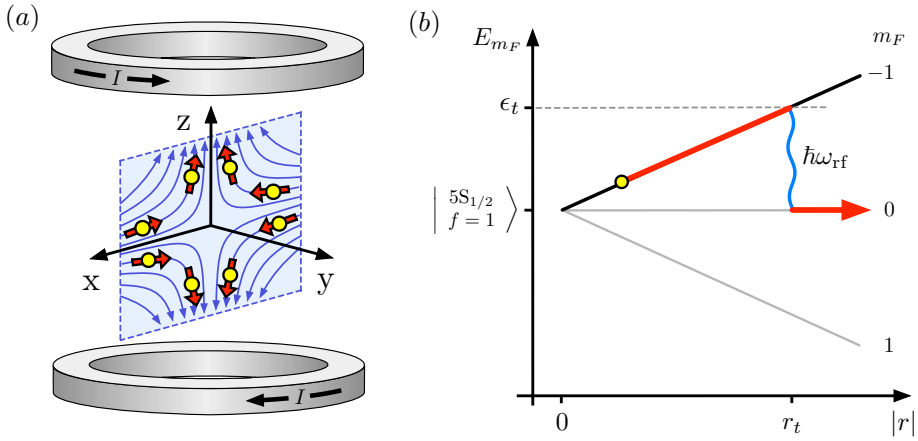

Figure 2.3: Magnetic confinement and driven evaporative cooling within a spherical quadrupole potential. (a) Spherical quadrupole coils producing the magnetic field cross-section represented in blue. Eight round particles are represented with arrows indicating the corresponding magnetic dipole orientations. Since each moment is equivalently aligned with the local field the sample is spin polarised, and will remain so while particles adiabatically move about the potential. (b) RF driven evaporation transition for the lower ground state in the linear Zeeman limit.

2.2.3 RF-Evaporation

Within conservative potentials evaporative techniques are required to induce cooling. The evaporation cools the cloud by removing atoms with above average energy, enabling the ensemble to rethermalise to lower temperature through inter-particle collisions. While this may always be achieved through gradual weakening of the potential, the corresponding reduction of thermalising elastic collisions makes this approach inefficient. In magnetic potentials however, the existence of non-trappable states permits a preferable alternative (figure 2.3b). While preserving the confining potential, RF fields may drive spin flip transitions at $\epsilon_t = \mu B = \hbar\omega_{RF}$. For efficient driven evaporation, characterised by an increasing trap density, the initial truncation parameter η should be large and the frequency lowered slowly [22].

$$\eta = \frac{\epsilon_t}{k_B T} \tag{2.14}$$

If the density increase is sufficiently large, that despite the decreasing temperature the elastic collision rate is increasing, then the evaporative process will continue to accelerate as the temperature drops. Known as *Runaway Evaporation*, this cooling regime is commenced by ramping the potential prior to the application of rf-fields. For the present method the field is ramped during transfer from magnetic to hybrid potential.

2.2.4 Majorana Loss

Within magnetic potentials atomic magnetic moments adiabatically follow the spatially continuous confining field. Although at locations of zero-field amplitude there exists a discontinuity, resulting in the random realignment of atomic moments through the region [34]. At high temperature and low density magnetic confinement, the quadrupole zero-field contributes negligibly. Conversely, for higher density confinement *Majorana Spin Flip* losses become prohibitively large. BEC within magnetic potentials therefore required the development of field geometries with non-zero minima. Both static and dynamic approaches were taken, with the *Ioffe-Pritchard* and *Time Orbiting Potential* (TOP) the most respectively successful. In the hybrid magnetic & optical trap being constructed, RF driven evaporation is expected to proceed down to $\sim 10\mu K$ before Majorana loss becomes significant [7]. At which point the $\sim 65\mu m$ diameter cloud will be transferred to the ODT. Note that since the magnetic field continues to provide longitudinal confinement, the quadrupole field zero cannot overlap the ODT. Instead the ODT waist is offset vertically $65\mu m$, the diameter of the transfer cloud, below the quadrupole zero.

2.3 Dissipative Optical Confinement

Observing comet tails point radially away from the sun, independent of velocity, the kinetic action of light radiation on matter was first proposed by Kepler in 1619. Over the next three centuries the hypothesis endured to influence classical theoretical work regarding the nature light. Despite many experimental attempts to probe radiation pressure, all suffered the disturbing action of surrounding gas. Not until 1903 was the phenomena first successfully demonstrated by Nichols & Hull, who used a torsion balanced Crookes apparatus with

variable internal pressure [35]. In this reference the authors additionally provide a comprehensive yet concise historical overview of earlier work. Radiation force on molecular gas was soon demonstrated thereafter through the detected change in containment pressure induced by light driven vortices [36]. Interest in radiative forces grew over the coming decades as a potential tool for the investigation of emerging relativistic [37] and quantum theories [38]. Achieving the velocities required for the observable manifestation of relativistic effects however proved practically challenging. Following the development of cathode ray technology with narrow velocity distribution, narrowband measurement of *Doppler* shifted atomic resonance spectra was demonstrated in 1938 [39]. During the 1960's space era, some focus was directed toward the influence of radiation on the trajectory of comets and life craft with larger planar surfaces [40–42]. Post moon landing in 1969, interest bolstered for the evolving investigation of quantum scattering interactions [43–45].

During this period it was demonstrated that radiation forces could themselves be used for the manipulation and investigation of systems on smaller scales than through existing means [44, 46]. Spontaneous emission, stimulated emission, and induced dipole forces where each initially identified as distinct contributions to the total radiation pressure [47]. The former two emissive actions are historically classified *Scattering* forces, and distinguished from the later comparatively weak non-emissive *Induced* force. Given the different optimal conditions for the manifestation of scattering and induced forces, continued work toward the formation of stable radiation traps diverged [48–51]. Stable optical confinement was first observed in 1986 focussing a single high-intensity far-detuned gaussian beam to induce sufficient dipole force [52]. Although initially considered plausible, many obstacles had been encountered toward stable scattering force confinement [53]. Subsequent theoretical work however demonstrated that no configuration of static light fields could manifest a stable scattering force [54]. Analogous to Earnshaw's theorem for coulomb potentials [55], this revelation became known as the *Optical Earnshaw Theorem* (OET). With supporting evidence mounting for OET [56], dynamic beam configurations were proposed as possible solutions [57]. However in 1986 it was realised OET need not apply to atoms with complex internal degrees of freedom [58]. Since electric or magnetic fields respectively Stark or Zeeman shift atomic spectra, resonant scattering rates may be spatially controlled with the application of non-uniform fields. To distinguish regimes circumventing OET, field stabilised scattering forces became known as *Spontaneous* forces. For a more recent historical review consult the 1998 Nobel laureate address [59].

Optical Molasses (OM) describes configurations of counter propagating cooling beams. Naturally the superposition of opposing fields form a standing wave and thus a spatially dependant field amplitude. Reactive forces therefore inherently influence the dynamics within OM configurations. *Magneto-Optical Traps* (MOT) additionally employ magnetic fields to induce spatially dependant scattering, thereby stabilising OM. Given the variety of possible geometries, externally applied magnetic fields facilitate greater control over the domain of spatial confinement. In this section these scattering potentials will be treated in greater depth, highlighting the advantages and limitations of confinement therein. An alternative method for loading MOT is then considered for the reduction of background collisional loss.

2.3.1 Optical Molasses

Proposed in 1975 [60] and demonstrated in 1985 [61], OM represents an enabling scattering force cooling regime. While most significantly predicating MOT, OM additionally facilitates optical pumping prior to magnetic confinement. *Classical Molasses* consist three counter propagating beam pairs along orthogonal axis. Generally these beams have equal intensity I and detuning Δ, away from atomic transition ω_0 with natural linewidth Γ. While rigorous three dimensional treatments are presented in [62–65], when the ground state occupation remains suitably unperturbed, the scattering for each beam may be treated independently. Consequently, well below saturation ($I \ll I_0$) the approach of [66, 67] demonstrates good agreement. Despite operational intensities typically exceeding saturation, the later approach will be presently adopted to illuminate the regime limitations. Consider an atom moving with velocity v_z between two counter propagating beams. With the positively labeled beam propagating toward z^+, the *Doppler Effect* contributes $\Delta^{\pm}$ to the effective detuning Δ_T of each stationary source in the atom rest frame.

$$\Delta_T = \Delta + \Delta_{\pm} \qquad \Delta_{\pm} = \mp k v_z \tag{2.15}$$

Hence for $\Delta < 0$ the oncoming beam will approach resonance, increasing the scattering rate $R_{\pm}$. Conversely, the mechanical contribution shifts the overtaking beam farther from resonance. The consequent recoil imbalance thereby constitutes a velocity dependant resistance. For each beam, the time averaged force $F_{\pm}$ is simply the product of photon momentum and scattering rate [68]. At suitably low intensity, the *Damping Force* (F_R) is then simply the addition of these independent scattering forces.

$$\begin{aligned} F_R &= F_+ + F_- \\ &= 4\hbar k \left(\frac{I}{I_0}\right) \left(\frac{\left(\frac{2\Delta|\Delta_{\pm}|}{\Gamma}\right)}{1 + 2\left(\frac{4\left(\Delta^2+\Delta_{\pm}^2\right)}{\Gamma^2}\right) + \left(\frac{4\left(\Delta^2-\Delta_{\pm}^2\right)}{\Gamma^2}\right)^2} \right) \end{aligned} \tag{2.16}$$

At low temperatures, one may furthermore reasonably impose $|\Delta_{\pm}| \ll |\Delta|$. Defining the *Damping Coefficient* (D_α), F_R is evidently proportional to velocity. Furthermore, from equation 2.17, the maximal damping force corresponds to the detuning $\Delta = -\Gamma/\sqrt{12}$. Solutions for equations 2.16 and 2.17 are presented in figure 2.4(a).

$$F_{R2} \approx \left[4\hbar k^2 \left(\frac{I}{I_0}\right) \left(\frac{(2\Delta/\Gamma)}{\left[1 + (2\Delta/\Gamma)^2\right]^2} \right) \right] v_z = \left[D_\alpha\right] v_z \tag{2.17}$$

For sustained cooling, atoms must cycle through the ground state via spontaneous decay. Given the sporadic emission distribution is spherically symmetric, the associated recoil averages to zero. However since the mean square recoil is non-zero, the damping force does not manifest unopposed. Rather, atoms traverse diffusive $p_{\pm}^2$ increment random walks through square momentum space, thereby increasing the average thermal energy. As the dynamics are now multi-dimensional, $n_z < 2$ is introduced to quantify the mean projected increment,

along a given axis per optical cycle. Maintaining the assumption of independent scattering, the mean square momentum change defines the *Momentum Diffusion Constant* (D_β).

$$\frac{d\langle p_s^2\rangle}{dt} = n_z \left[p_\pm^2 \left(R_+ + R_-\right)\right] \approx 2\left[D_\beta\right] \tag{2.18}$$

At thermal equilibrium the competing damping and diffusive effects balance, and the characteristic *Doppler Limit* (T_D) represents the minimum achievable temperature via optical scattering. In contrast to the condition for maximal damping, T_D is obtained for $\Delta = -\Gamma/2$. For the ^{87}Rb cooling transition $T_D = 146\mu$K.

$$T_D \;=\; \frac{h\Gamma}{2k_B} \tag{2.19}$$

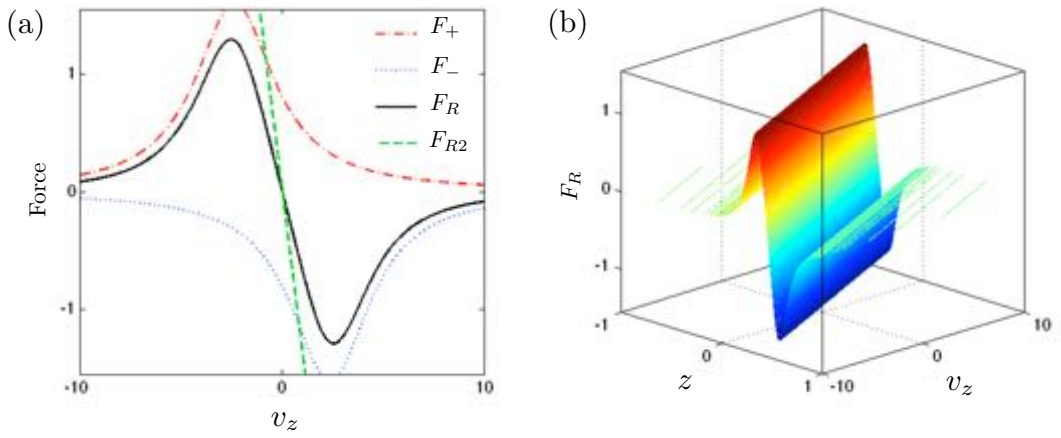

Figure 2.4: Damping forces within classical (a) optical molasses, and (b) magneto-optical traps. Represented are the solutions for equations 2.16 and 2.17, with effective molasses and MOT detuning respectively described by equations 2.15 and 2.21. Presented for $I/I_0 = 0.01$, note these solutions are valid only in the low intensity limit. Consist with the requirement for achieving minimum temperature T_D, the source detuning $\Delta = -\Gamma/2$ was used. Furthermore within (b), the magnetic field gradient $b = 2$ T/m is on the order of existing systems [7]. All forces are in $10^{-22}N$, distances in mm, and velocities in m/s.

2.3.2 Sub-Doppler Cooling

In 1989 the observation of bimodal velocity distributions for intermediate beam intensities indicated the existence of a secondary cooling mechanism within classical molasses [69]. Furthermore, the second velocity group demonstrated an uncorrelated dependance on Δ, beam misalignment and imbalance, polarisation, and external fields. Curiously, some misalignment angles were even demonstrated to enhance the *Sub-Doppler* velocity distribution. Of greater theoretically significant however was the substantial dependance on the cooling beam polarisation. Through a series of polarisation specific treatments, four canonical configurations were considered [70–72], for which the standing optical fields are presented in figure 2.5.

While the previous treatment of classical OM neglected these *Polarisation Gradient* effects, temperatures approaching the *Recoil Limit* (T_R) may be achieved in optimal conditions [73]. For the ^{87}Rb cooling transition $T_R = 360$nK.

$$T_R = \frac{\hbar k^2}{2mk_B} \tag{2.20}$$

For the $\sigma^+\sigma^-$ configuration the standing optical field is everywhere linearly polarised with equal amplitude. Spatially invariant Stark shifts therefore preclude all discontinuous cooling mechanisms manifest within other canonical configurations. Instead consider a reference frame translating with the atom and which rotates to preserve the orientation of the local optical field. Given the frames rotation an inertial field exists within ($\mathcal{H}_{\text{rot}} = kv\mathbf{J}_z$). This inertial contribution to the effective hamiltonian then induces a velocity dependant Zeeman shift, promoting absorption of the oncoming beam polarisation for $\Delta < 0$.

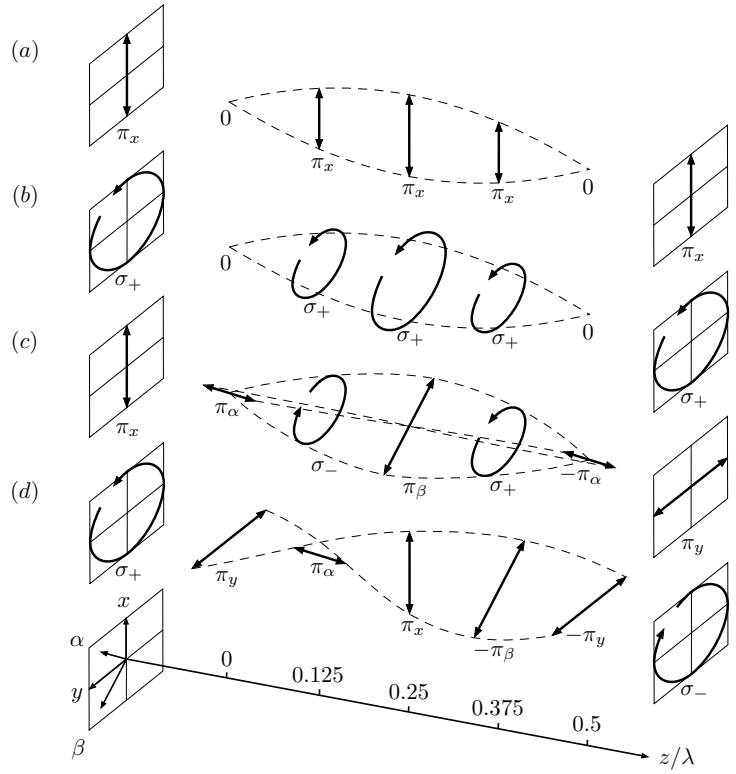

FIGURE 2.5: Optical molasses standing fields for canonical polarisation configurations. While three orthogonal beam pairs are typically employed, the sub-doppler cooling mechanisms may be extrapolated from the one-dimensional treatment. On opposing grids the polarisation of inwardly counter-propagating cooling beams are represented. Between grids the equal intensity standing fields are represented. $(a-b)$ require a uniform magnetic field to induce spatially dependant competition between Larmor precession and spin polarising transitions. (c) passing between adjacent circularly polarised domains spin polarised atoms experience Stark induced forces. (d) motion induced Zeeman effects partially spin polarise the sample to promote asymmetric scattering.

2.3.3 Magneto-Optical Trap

Within classical OM, atoms experience velocity dependant resistive scattering forces. Since the doppler mechanism is spatially invariant however, the resultant cooling merely reduces the diffusive loss rate. Within a magnetic spherical quadrupole however, the Zeeman effect additionally induces a spatially dependant detuning Δ_B (figure 2.6b). Notice that contrary to the magnetic quantisation convention, states are here defined relative the axis along which the interacting optical beam propagates. Hence although adiabatic motion across the trap would preserve the local orientation, relative the coordinate system the state would be flipped. Furthermore, the six beam polarisations are selected to preserve the internal state of oncoming particles. Comparing figures 2.6a & 2.3a it should be apparent that the MOT transition states are not magnetically trappable. While magnetic forces are negligibly weak compared to optical scattering, using non-trappable states does necessitate optical pumping during the transfer from MOT to Magnetic trap. However to optically pump the transition $|f = 2, m_F = -2\rangle \rightarrow |f = 1, m_F = -1\rangle$ the repump need only be blocked momentarily before the cooling light, since the repump is purposed to reverse this transition. While determining particle dynamics requires computational methods, insight may be gained considering the relative magnitude of the detunings Δ_B and Δ_E, respectively induced by the magnetic confinement field and optical standing waves. Within a magnetic spherical quadrupole, the problem thus naturally separates into the consideration of core and shell domains, separated by the $\Delta_B = \Delta_E$ boundary of radius r_R [74, 75]. Hence within MOT there exist two spatially distinct regions, for which either the loading or density is optimised.

$$r_R \approx \left(\frac{\hbar\Gamma^2}{2\Delta\mu_B b}\right)\left(\frac{I}{I_0}\right) \tag{2.21}$$

For atom numbers $N < 10^4$ MOT typically fit entirely within the optically dominated core. In this *Temperature Limited* scheme atoms behave as an ideal gas. Conversely, within MOT extending into the shell, photons may scatter multiple times before escaping the cloud, thus appropriately named the *Multiple Scattering Regime*. The consequent repulsion between atoms decreases cloud density, and via momentum diffusion and field interference suppresses sub-doppler cooling within the core. Once $N > 10^8$ the shell occupation is sufficiently large to dominate the core and raise the minimum achievable temperature to T_D. MOT of the later size are additionally limited to $n = 10^{10} - 10^{11}$ cm^{-3} and $\rho \approx 10^{-6}$ [76], thereby precluding BEC within dissipative scattering potentials. In preparation for loading into conservative potentials however, small density and temperature gains may be achieved. For the present approach a *Compressed MOT*, alternatively known as a *Temporal Dark MOT*, will be implemented. This involves substantially reducing the outward radiation pressure, by decreasing both cooling & repump beam intensities, and increasing the detuning. Simultaneously ramping the magnetic field increases trap density by forcing atoms toward trap centre [77–79]. Since this process is transient, rapid magnetic recapture is required immediately following this procedure to preserve the increased phase space density.

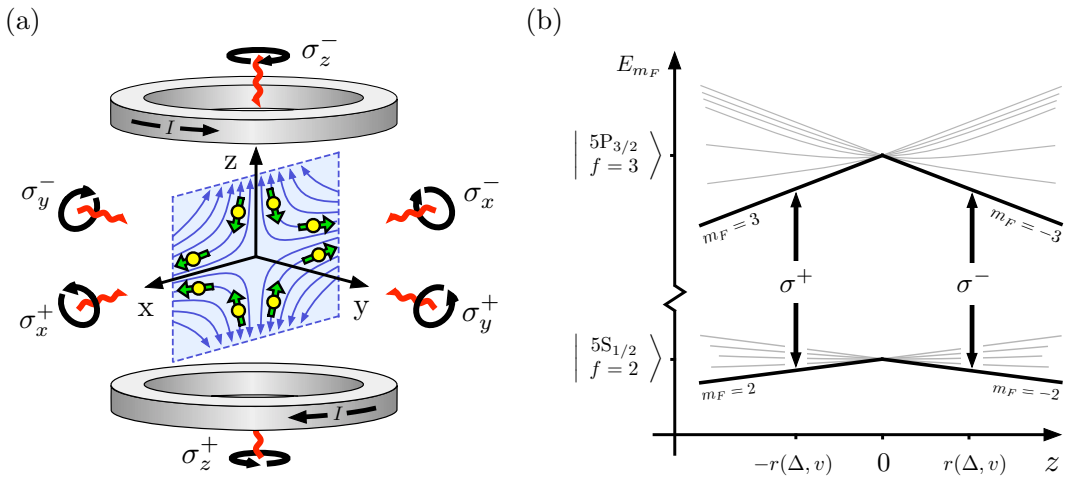

FIGURE 2.6: Spherical quadrupole MOT configuration and hyperfine transitions. (a) Standard configuration consisting antihelmholtz current loops and three orthogonally arranged counter propagating beam pairs, each $\sigma^+\sigma^-$ configured. Six yellow particles in the $|5S_{1/2}, f = -2\rangle$ state are represented on the blue magnetic field line cross-section. Green arrows representing the atomic magnetic moments are all locally anti aligned with the magnetic field, representing the locally defined $|m_F = -2\rangle$ substate. Notice that contrary to the magnetic quantisation convention, states are here defined relative the central coordinate axis. Hence although adiabatic motion across the trap would preserve the local orientation, relative the coordinate system magnetic moments revolve. (b) Zeeman shifted substate energies consistent with the Breit-Rabi formulae and the numeric derivation of [17]. Bold lines represent the transition states which, by the global quantisation convention, are represented with the opposite sign for $z < 0$. Since the global polarisation of optical fields is conversely fixed, each beam only interacts with particles displaced & moving toward them.

2.3.4 MOT Loading

Increasing the number of particles within the final condensate requires greater initial loading, increased cooling rate, or a reduction in loss rate. The later will be considered here. From section 2.1.3 single-body background collisional loses contribute most significantly, thereby motivating *Ultra-High Vacuum* (UHV) conditions. However, since conventional MOT load direct from a thermal vapour, *High Vacuum* (HV) load pressures are required. Condensation under UHV therefore necessitates rapid evacuation of the surrounding chamber each cycle following the MOT load. While representing a great strain on the pump system, shortening the operational life, practically the desired pressures cannot be obtained within characteristic cycle times. The solution is to employ an alternative load mechanism which enables UHV conditions to be maintained. Atom beam loading satisfies this criteria (figure 2.7). From an adjacent chamber a collimated atom beam may pass through a narrow feedthrough to load MOT under UHV conditions. Many technologies have been developed for atom beam formation, including the *Zeeman Slower* [80] and *Low-Velocity Intense Source* (LVIS).

$$N(t) = \frac{\delta}{\alpha}\left(1 - e^{-\alpha t}\right) \tag{2.22}$$

For the present work however a $2D^{+}MOT$ system will be employed [81]. To model the load process for diagnostic purposes, consider the rate equation 2.9. For typical load densities we may reasonable neglect two and higher body losses [82]. Solving the rate equation for $\beta = \gamma = 0$ produces equation 2.22.

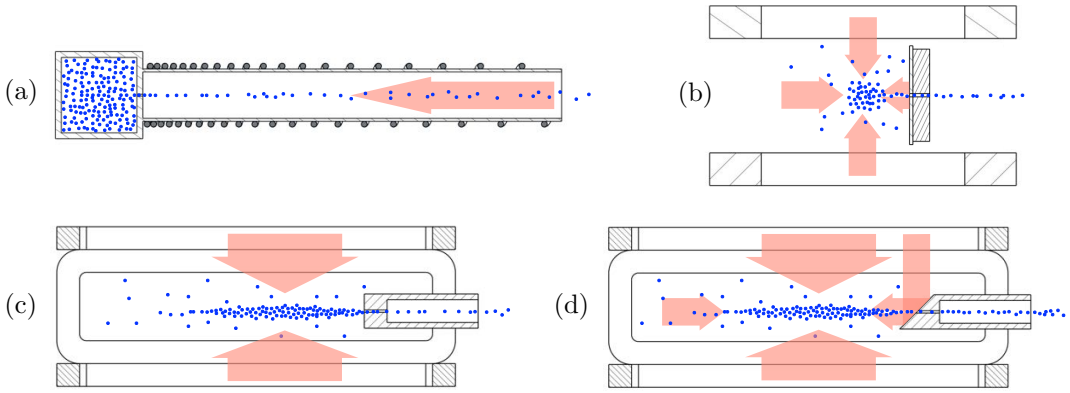

Figure 2.7: Atom beam regime cross-sections. Confinement in the third dimension orthogonal the page is equivalent to the vertical mechanism in each case. (a) Zeeman Slowers induce a magnetic detuning to directly cancel the doppler detuning [83]. To keep the atoms resonant as they decelerate along the beam path the field is spatially varied by extension of the solenoid pitch. (b) LVIS are an early 3D-MOT adaption which uses a quarter waveplate with mirrored back to reflect the horizontal beam with opposite circular polarisation [84]. A narrow hole through the plate centre omits the reflected light over that area creating the necessary imbalance to accelerate particles. (c) 2D-MOT scheme with favourable geometry for beam formation.[85]. (d) $2D^{+}$MOT incorporates elements of (b-c) to drive the atom beam with controlled mean velocity and smaller variance, while reducing the beam divergence [86].

2.4 Reactive Optical Confinement

First experimentally distinguished from the resonant scattering force 1978 [51], induced optical force potentials have since developed for many diverse purposes outside cold atom physics. Applications include, the manipulation and manufacture of carbon nano tube microstructures [87], and probing the mechanical behaviour of red blood cells [88]. The great appeal of *Optical Dipole Traps* (ODT) for these tasks is they are non-invasive and easily controlled. Unlike scattering force potentials, ODT are conservative, meaning they induce comparatively little heating, but retain the advantage of spatial flexibility over magnetic potentials. For the present discussion the *Stark Effect*, which physically mediates ODT restoring forces, will be initially considered. Gaussian ODT geometries relevant for the principle investigation will then be identified and summarised.

2.4.1 Stark Effect

Analogous to the Zeeman Effect induced by magnetic fields, electric fields provide an additional mechanism for lifting the degeneracy of hyperfine substates. Rather than interacting with the existing magnetic moments however, the field induces an electric dipole between the electron cloud and nucleus. The *Stark Effect* hence describes the non-uniform interaction of an electric field with the atomic charge distribution.

$$\mathcal{H}_E = -\boldsymbol{\mu}_E \cdot \mathbf{E} \tag{2.23}$$

Since generally the electric dipole is simply proportional to the inducing field, the present description requires solving for proportionality factor α_E, known as the *Complex Polarisability*. For static fields the solution may be derived from considerations of transition state parity [89], and the algebraic formalism of spherical tensors [90]. A spin dependant expression for α_E results, requiring the definition of transition specific *Scalar* and *Tensor Polarisabilities*, α_0 and α_2 respectively. Energy shifts induced by static fields and thus consistent with this theory encompass the *DC Stark Effect*.

$$\boldsymbol{\mu}_E = \alpha_E \mathbf{E} \tag{2.24}$$

Of greater practical interest however, contrast with the static magnetic consideration, are the oscillating electric components of optical fields. In the time dependant treatment, equation 2.24 represents an amplitude expression. Three energy scales are relevant for this problem, which in descending order are, the excited state fine structure splitting Δ'_{FS}, ground state hyperfine splitting Δ_{HFS}, and excited state hyperfine splitting Δ'_{HFS} (figure 2.1). Generally in multi-level atoms all three contribute to the transition probability and induced force. On energy scales exceeded by the optical detuning Δ however, the distinction between non-degenerate states becomes less significant. Consequently for large optical detuning compared to the excited state fine structure splitting ($|\Delta| \gg \Delta'_{\mathrm{FS}}$), the interaction potential $\mathcal{H}_E$ is derived [24].

$$\mathcal{H}_E = \left(\frac{3\pi c^2}{2\omega_0^3}\right)\frac{\Gamma}{\Delta}\left(1 + \frac{\mathcal{P}}{3} g_F m_F \frac{\Delta'_{\mathrm{FS}}}{\Delta}\right) I \tag{2.25}$$

$\mathcal{P}$ quantifies the polarisation, taking the value 0 for linear fields and ± 1 for $\sigma^{\pm 1}$ circular polarisations. Δ represents the detuning of the optical field from the resonant frequency for the transition between the hyperfine ground state and the mean excited state energy. Γ is the resonant scattering rate, and I the spatially dependant optical intensity of the oscillating field. Alternatively, equation 2.25 may be interpreted as the ground state *AC Stark Shift*. The problem thus essentially treats a two level atom, since for large detuning we suitably ignore the excited state substructure. And since well below saturation atoms dominantly occupy the ground state, equation 2.25 well represents to total potential. Additionally notice that for linearly polarised optical fields the potential is spin invariant. Furthermore, the corresponding scattering rate Γ_ω for this regime provides the second expression of fundamental importance.

$$\Gamma_\omega = \frac{1}{\hbar}\left(\frac{\Gamma}{\Delta}\right)\mathcal{H}_E \tag{2.26}$$

One firstly concludes that for red-detuning ($\Delta < 0$) the potential is minimum for maximum intensity, with the reverse true for blue detuning. Hence two classes of far detuned *Optical Dipole Trap* (ODT) exist. Secondly, while the potential scales with I/Δ and scattering scales as I/Δ^2. Strong conservative confinement with far detuned beams is therefore experimentally limited by the available laser power.

2.4.2 Optical Dipole Trap

While equation 2.25 identifies two classes of far detuned ODT, only attractive red-detuned ($\Delta < 0$) potentials will be presently discussed. A single focussed gaussian beam (figure 2.8a), characterised by transverse intensity profile $I(r, w)$, is the simplest example.

$$I(r, w) = \left(\frac{2P}{\pi w(z)^2}\right) \exp\left(\frac{-2r^2}{w(z)^2}\right) \tag{2.27}$$

Here P represents the laser power, r the radial distance for the beam axis, and w the radius the intensity decays to e^{-2} its value on the propagation axis z. Confinement is therefore strongest at the focus, where the *waist* (w_0) is minimal. Passed through a single focal length f lens, a collimated beam with diameter D will form the following waist.

$$w_0 = \frac{2\lambda}{\pi}\frac{f}{D} \tag{2.28}$$

For single beams w_0 uniquely describes the trapping potential. This includes the strength of longitudinal confinement, which is characterised by the *Rayleigh Length* (z_R).

$$z_R = \frac{\pi w_0^2}{\lambda} \qquad w(z_R) = \sqrt{2} w_0 \tag{2.29}$$

Since the longitudinal confinement is much weaker ($z_R \gg w_0$) however, many hybrid potentials have been developed. While the method developed in this thesis uses a secondary magnetic potential (figure 2.8b), suitable all-optical solutions have also been demonstrated (figure 2.8c). Of particular interest for interferometry is the *Scanned ODT* potential in figure 2.8d. This potential consist a cylindrically expanded gaussian beam, called a *Sheet*, which aligned horizontally provides strong one-dimensional confinement against gravity. Moving a second orthogonal beam thus enables the formation of arbitrary two dimensional *Time Averaged Adiabatic Potentials* (TAAP). Present work is conducted with the view of transferring BEC into a ring potential of this type.

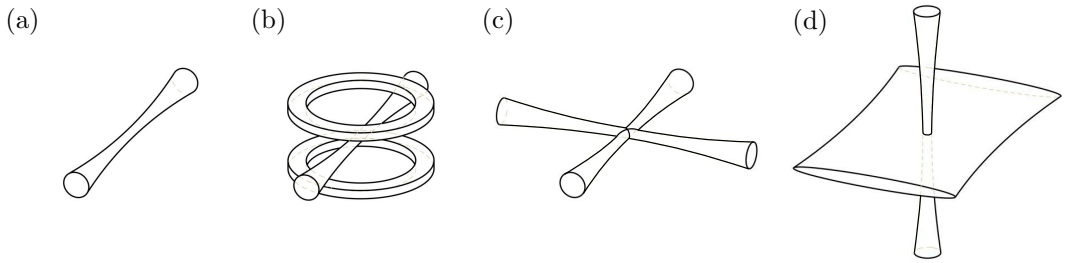

FIGURE 2.8: Hybrid optical dipole trapping configurations. All potentials employ negatively detuned far off resonance gaussian beams, inducing conservative confinement at optical intensity maxima. (a) simplest gaussian ODT regime providing only weak longitudinal confinement [25]. (b) magnetic spherical quadrupole enhanced longitudinal confinement. (c) *Crossed ODT* where orthogonal linear polarisations are required [91]. (d) *Scanned ODT* facilitating the flexible generation of two-dimensional TAAP [92].

3 Experimental Design

3.1 Vacuum System

3.1.1 Construction

Since single-body collisional losses (α) with the thermal background dominate at high pressure, high vacuum environments are essential for extending trap life and increasing atom number. The ultimate success of condensate regimes therefore critically depends on the initial vacuum design, something not easily adjusted. While *Ultra-High Vaccum* (UHV) conditions approaching 10^{-11} mBar or lower are ideal, neutral atom experiments require a vapour source typically at *High Vacuum* (HV) pressures around 10^{-7} mBar. Hence single chamber systems forming condensates within the vapour cell must repeatedly pump down the background following an initial loading period. While this high continuous pump load shortens the operational life, the difficulty of reaching UHV quickly often means ideal pressures cannot be reached during each cycle [12]. This motivated the development of two stage regimes, where low divergent atomic beams, formed under HV, load the adjacent UHV trap via a low conductance feedthrough. The designed vacuum system consequently consists two independently pumped volumes (figure 3.1). A specially machined copper gasket internally separates the regions, extending a mirrored feedthrough appropriate for $2D^+$MOT into the vapour cell.

HV Section The vapour cell has four rectangular windows to permit the transmission of two cylindrically expanded $2D^+$MOT cooling beams. The square cross-sectional width is 25.4mm to match the 1inch collimating optics. On the tee end of this cell the heat treated copper gasket is specially machined to include the feedthrough separating the partitions. As the cell must be attached on both ends, a flexible bellows is essential to prevent breakage during the assembly process. The later tee piece contains the rubidium dispenser, and is

therefore importantly positioned closest the cell. Furthermore, no direct line between the dispenser and the Gamma Vac 10S ion pump exist. This second feature prevents Rb accumulating on the pump electrodes, which would reduced both pump and dispenser filament lives. Through the view port on the pump tee a *Push Beam* is used to increase loading into the UHV section. The valve facilitates temporary attachment of a turbo pump necessary for initial pumping and during baking.

UHV Section The science cell consists seven octagonally arranged 25.4mm diameter and two 40mm diameter windows. All of which are double AR-coated and bonded to a machined quartz body. Below the connecting tee a 6inch cross houses an Agilent titanium sublimation pump, mounted vertically through the bottom port. The 240mm shaft of this pump extends to the top surface of the cross, meaning the 100mm titanium elements occupy the top half. An important consideration for this placement was the relative position of the Varian Starcell ion pump. Since the sublimation pump works by layering the surround chamber walls with reactive titanium, no direct line should exist between the sublimation element and the ion pump. Both pumps are required however since the complimentary mechanism together facilitate sustained UHV conditions. As the control box for the Varian ion pump does not provide a convenient pressure reading, an Agilent ionisation gauge was additionally added to the remaining port of the 6 inch cross.

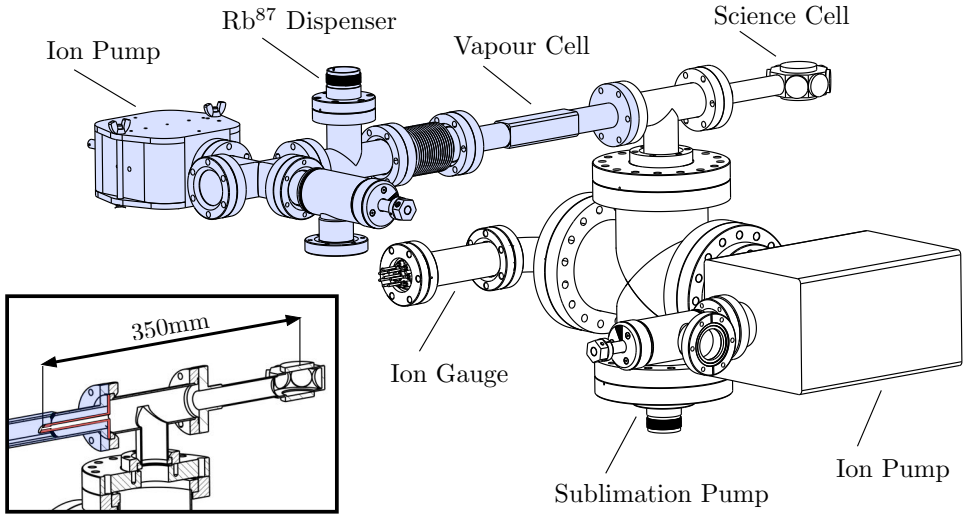

FIGURE 3.1: Two chamber vacuum system internally partitioned with a low conductance feedthrough, which is of the form appropriate of $2D^{+}$MOT. The feedthrough entry is 1.2mm in diameter 12mm long, after which the internal passage broadens. [Blue] During operation the dispenser floods this section with thermal rubidium vapour. About the transparent vapour cell region a $2D^{+}$MOT system may pass a collimated beam atoms via the feedthrough into the science cell. The ion pump is a Gamma Vac 10S. [White] UHV conditions are maintained in this section using a Varian Starcell ion pump and Agilent titanium sublimation pump. The octagonal science cell windows are deigned to provide sufficient optical access for MOT and ODT optics, while additionally facilitating close proximity imaging and magnetic field generation.

3.1.2 Bake Procedure

As ion pumps are only suitable for use below around 10^{-6} mBar, alternative pumping methods are initially required from atmospheric pressure. Generally two stages processes are necessary, where the exhaust of the primary pump is itself pumped in series. The standard configuration consists a primary *Turbo* pump supported by an atmospheric pressure pump. Initially the system is pumped through the idle turbo pump to the terminal pressure of the support pump. For the present work a scroll pump was used, for which the pressure plateaued around 10^{-2}mBar. The primary turbo pumps are then engaged, plateauing around 10^{-7} mBar. While two turbo pumps were required to evacuate each side of the feedthrough, the single scroll pump capably supported both. Although this pressure is within the operational range, the ion pumps are not immediately used. Despite cleaning vacuum parts of residual oil and particulate matter, gases at atmospheric pressure leach into stainless steel, a process reversed once the pressure is reduced. Constituting a form of leakage, accelerated expulsion under the pumping action of the turbo pumps is ideal. For this purpose the system is encased in heating cables, thermocouples and insulating aluminium foil, in a process known as *Baking*. For maximal effect each component is maximally heated within its limit. Naturally glass and other non-metal components may not reach the same temperature as stainless steel, and therefore take longer to bake. Higher temperature all metal bakes are therefore commonly used to more rapidly outgas the metal majority. Hence initially the system was constructed using a blank flanges, nitrogen valve, and two nipples for the view ports, science and vapour cell respectively. Baking above 300°C the pressure plateaued back around 10^{-7} mBar after ten days (figure 3.2). Cooling the system subsequently resulted

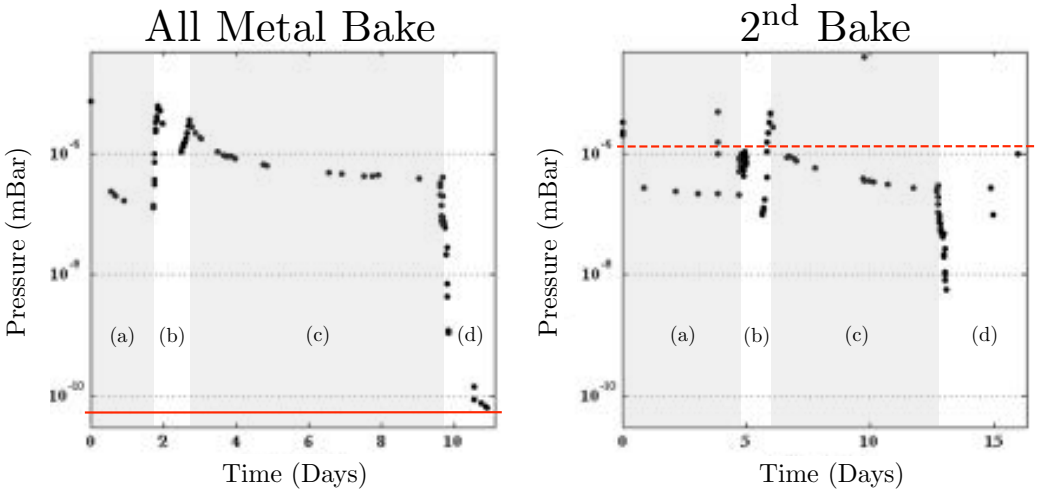

Figure 3.2: Representative pressure data recorded for the first two of five bakes. For comparison of the two plots four distinct regions are identified. (a) Turbo pump down. (b) Heating period where temperature gradients across glass components must be avoided. (c) Extended bake at maximum temperature until pressure plateau. (d) Cooling & operation of final pump configuration. In the later bake the initial pressure drop in (d) was thermally driven. The existence of a leak however subsequently resulted in final pressure around 10^{-6} mBar, substantially greater than the 10^{-11} mBar achieved in the first and final bakes. The red lines represent these pressures.

in another half order drop in pressure. The ion gauge and sublimation pump were each then degassed, resulting in a temporary pressure spike. To reduce reabsorption bringing the pressure back to atmosphere, the system was flooded with nitrogen prior to the exchange of non-metal components. The bake procedure was then repeated below 150°C over a period of 15 days. Unfortunately the terminal pressure achieved was only 10^{-6} mBar indicating the existence of a leak. Replacing the backing pump with the helium leak detector helped resolve two leaks over the course of three subsequent bakes. In removing the ion pump magnets between bakes it was found the supporting gasket had been strained. The specially manufactured feedthrough gasket was also leaking. Fortunately both leaks were resolved through further tightening on the join. The final pressure achieved for the closed system under ion and sublimation pumping is on the order 10^{-11} mBar, and therefore below the reasonable measurement capability of both the Gamma pump and Agilent ionisation gauge.

3.2 Laser Distribution

Acousto-Optical Modulators (AOM) represent an important experimental technology, facilitating microsecond optical switching and laser frequency shifts on the order 10^2MHz [93]. Since the difference between MOT cooling and repump frequencies is more than an order larger however, two independent lasers are required (figure 3.3). While the details of this system are beyond the present scope, a suitable treatment is provided in [12].

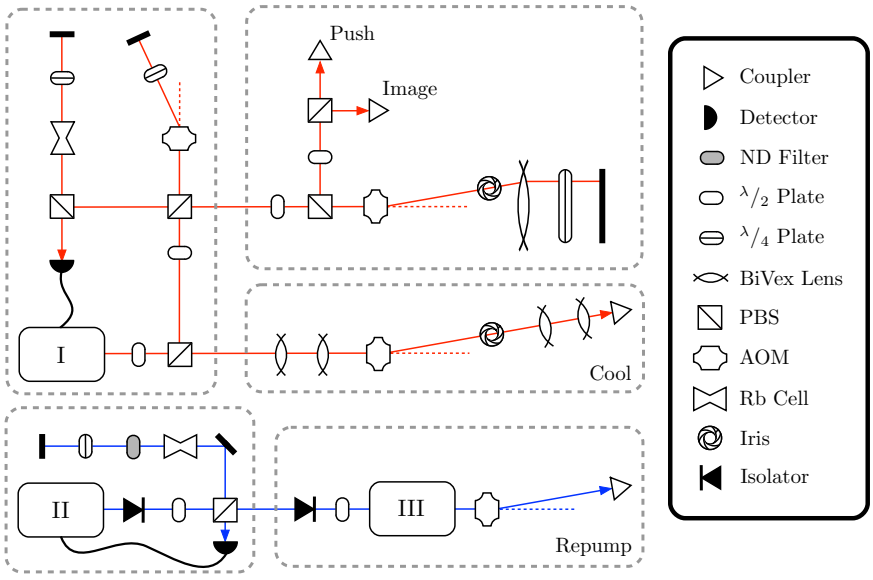

FIGURE 3.3: MOT laser system. (I) 1W Tropica TA-Pro diode cooling laser feed-back locked 320MHz above the $(f = 2, f' = 2, 3)$ cross-over resonance. For a final detuning 15MHz below the $(f = 2, f' = 3)$ transition the cooling beam AOM reduces the frequency by 201.7MHz. (II) 40mW Tropic DL100 diode repump laser, resonant locked on the $(f = 1, f' = 1, 2)$ transition. As this laser supplies three separate cold atom experiments the signal is amplified using the injection locked 500mW Tropica DLX110 amplifier (III).

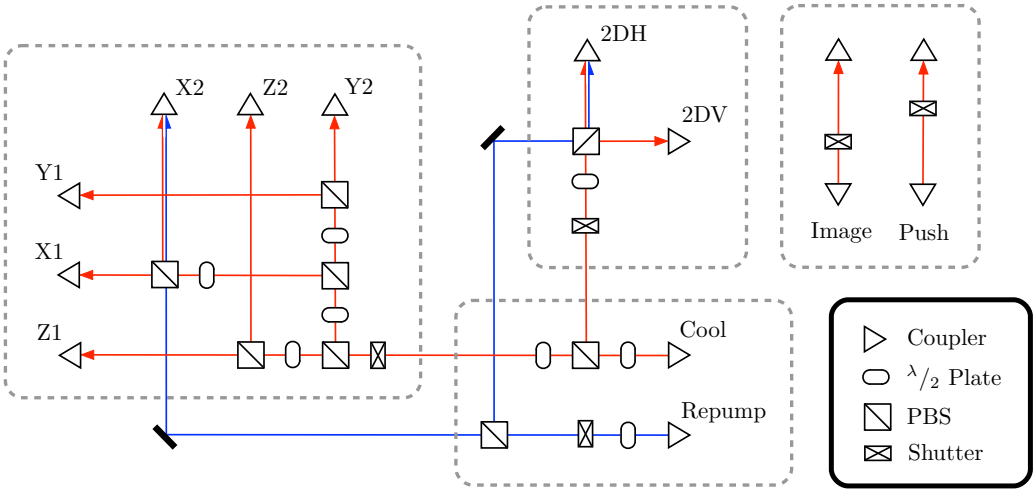

FIGURE 3.4: MOT optics laser distribution board. Receiving four input fibres from the laser table this board represents the final means of automated control. All output fibres here pass directly to the experiment through fixed alignment collimation optics. Two irises are included to assist with aligning the repump beam to follow the cooling beam. Five shutters additionally enable individual control and guard against leakage from the laser table.

Most importantly, four optical fibres exit the laser system and pass to the MOT distribution board (figure 3.4). From the single cooling input, a series of half wave plates and *Polarising Beam Splitters* (PBS) divide the cooling input into two 2D-MOT and six 3D-MOT output fibres. Alternatively, the repump light is injected into a single coupler for each MOT. Given the comparatively weak interaction with this frequency, uneven distribution does not adversely affect the MOT behaviour. Single coupler injection does however simplify the measurement of repump power into each MOT. The second most important feature of the distribution board are the five optical shutters. Mechanical shutters are required since although fast, small but ultimately destructive light quantities sill couple through off AOM. However, the vibration induced by the operation of mechanical shutters is sufficient to decouple diode lasers, precluding use as part of the laser system in figure 3.3. For the present work the shutters were uniquely manufactured using electrical relays, a design discussed in more thoroughly in appendix A.

3.3 2D-MOT

3.3.1 Coil Design

Cold and low divergent atomic beams represent an important tool for loading 3D-MOT under UHV conditions. While Zeeman Slowers and LVIS regimes have each been demonstrated, 2D-MOT and the derivative 2D$^+$MOT represent simpler and more efficient alternatives. Consisting two orthogonal counter-propagating beam pairs the base 2D-MOT provides no axial confinement or acceleration. The 2D$^+$MOT however additionally includes a third pair

along the axial direction, accelerating the atomic beam toward the secondary chamber. For the present experiment the goal is to develop a 2D-MOT regime with the capability of forming 2D$^+$MOT if later desired. The essential design incorporates aspects from two primary sources [85, 86], which both generate a transverse field gradient around 16 G/cm. While close proximity coil mounting reduces the required current, cooling beam optical access must be maintained. Consequently the inner diameter of the mounted coils should equal the 25.4mm vapour cell width. Using larger diameter enamelled wire additionally reduces the required current, although greater rigidity makes hand winding more difficult, typically resulting in a poorer package ratio. 0.615mm diameter enamelled wire was chosen as a compromise for the present design. Using the free-source Radia package for Mathematica the final coil design was developed (figure 3.6). With 40 turns per coil and 0.44 packing ratio, this design produces a transverse gradient of 4.12G/cm/A. A required current of 4A is expected, which for the calculated resistance 0.271Ω, would mean each coil generates 4.3W. Systematic cooling should therefore not be required.

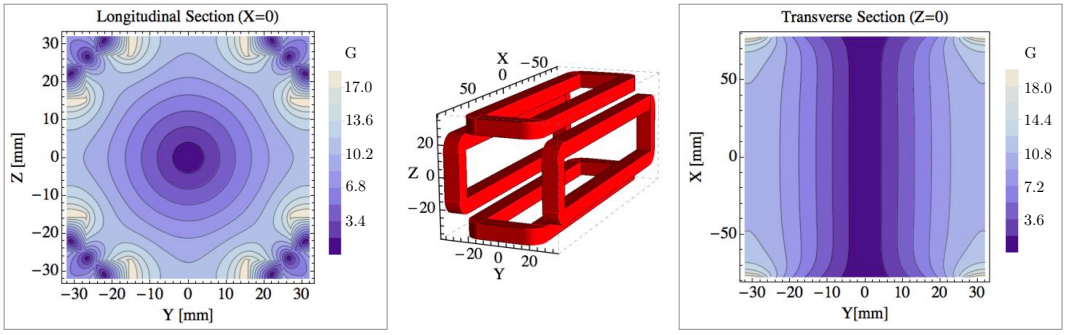

FIGURE 3.5: 2D-MOT coil design and field topography. For 40 turns per coil consistent with a packing ratio of 0.48 a transverse gradient 4.12 G/cm/A is generated. Hence negligible confinement is provided in the longitudinal direction while a sufficient transverse field is generated with approximately 4A. Since each coil has a resistance of 0.271Ω, each coil generates 4.3W of heat. A cooling system was therefore deemed unnecessary. For this design 0.615mm diameter enamelled copper wire was used.

3.3.2 Construction

This system was originally constructed with the magnetic coil supported on the same breadboard as the optics. The motivation behind this design was to maintain the relative alignment between the coils and optical field. Since one of the parameters to be optimised is the forward back location of the beam centre relative the end of the copper feedthrough, this mounting was intended to reduce the amount of realignment required. In reality however each time either system was adjusted both required attention. The other major drawback was the expanding cylindrical optics were mounted separately on the supporting breadboard, ensuring any adjustment necessitated realignment. In addition, mounting the divergent cylindrical lenses directly on the collimation optics made optical intensity measurements difficult. Ensuring the divergent lenses where equidistant from the large collimating lens

was an additional challenge. Consequently the system was redesigned to facilitate easier alignment and optimisation (figure 3.6). First the coil formation is mounted independently from the feedthrough vacuum flange. To remove any possibility of straining the vapour cell, mounting the coils from both ends was decided against. Furthermore, all the optics are now mounted on a single board, with the divergent cylindrical lenses not directly attached to the collimation optics. Since this required mounting the board atop those supporting, the vertical retroreflector needed to be slung beneath.

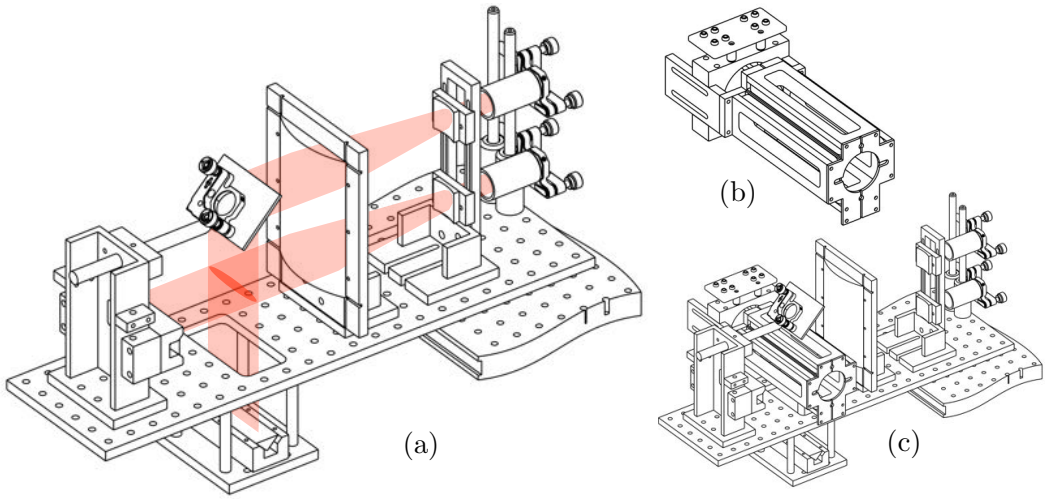

FIGURE 3.6: 2D-MOT physical construction. (a) Cooling light from the distribution board enters each lens tube via *Polarisation Maintaining* (PM) optical fibre. Before the $f = 50$mm collimating lens each beam is additionally passed through a quarter wave-plate. While the final beam helicities must be orthogonal, the vertical beam undergoes a polarity inverting reflection, hence both collimators are polarised identically. Beams are then cylindrically expanded through $f_1 = -50$mm then $f_2 = 200$mm lenses, horizontally broadening by a factor of four. To produce the opposing beams prism retro-reflectors are used to both reverse the propagation and maintain the correct polarisation. This method is simpler than expanding two additional beams, and substantially cheaper than uses large rectangular wave plates with planar mirrors. (b) The four magnetic coils are together supported by the feedthrough vacuum flange. (c) Relative position of the elements (a-b) in the final mounted design.

3.4 3D-MOT

3.4.1 Coil Design

Since the 3D-MOT coils are additionally employed for magnetic confinement, much of the following design is dictated by the higher demands of the later regime. Given the condensation method and reported atom numbers in [7] match those presently desired, this paper is considered a reasonable indicator of the experimental parameters required for 3D-MOT and

later confinement stages. Consequently longitudinal gradients of 12G/cm for MOT and 48-160G/cm for ramped magnetic confinement constitute the design requirements. Again using the Mathematica based Radia package the spherical quadruple coil design was developed (figure 3.7). Given the greater spatial constraints about the science cell, Laminax Flat Conducting Ribbon was considered instead of the round-section wire as it had a superior packing ratio. With 90 turns per coil and 0.75 packing ratio a longitudinal gradient of 4.93 G/cm/A was predicted. Hence the currents required for MOT and ramped magnetic confinement are therefore 3A and 10-33A respectively. Given the total series resistance of the four coils is 0.48Ω, maximum power associated with the ramped series current is 522W. Systematic cooling in this case is therefore necessary. A cooling system could furthermore permit greater currents, thereby facilitating future investigation into high field strength phenomena such as Fesh-Bach Resonances. For cooling purposes the thermally conductive surface of both coils has been doubled using stacked 6.35mm wide ribbon, with a 2mm separation. Both the top and bottom pair may then be mounted within sealed casings, through which cooling water is cycled. Operating as singular coils, each pair was modelled in parallel.

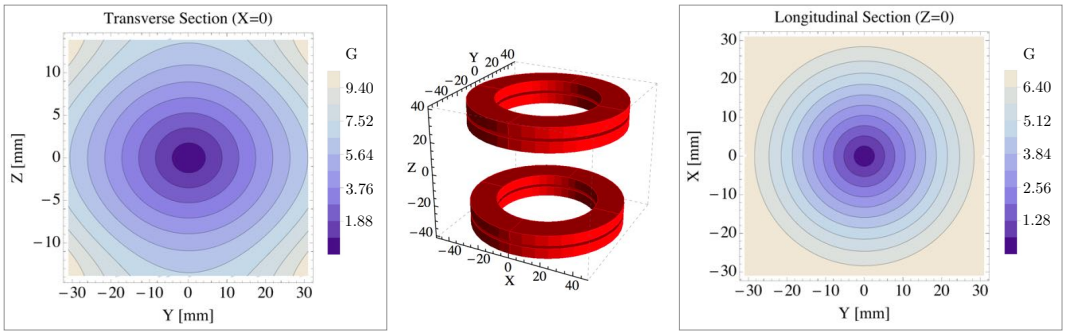

FIGURE 3.7: 3D-MOT coil design and field topography. For 90 turns per coil consistent with a packing ratio of 0.75, a longitudinal gradient 4.93 G/cm/A and transverse gradient 2.41 G/cm/A are generated. For 3D-MOT and ramped magnetic confinement respectively, the required currents are therefore 3A and 10-33A. For a total series resistance of 0.48Ω, the four coils together generate 522W at maximum ramp. Magnetic confinement thereby requires systemic cooling. Dividing quadrupole coils in two the thermally conductive surface area and therefore cooling rate are increased. For this design 6.35mm wide Laminax Flat Conducting Ribbon was used.

3.4.2 Coil Winding

To enable firm uniform winding of the four quadruple coils the apparatus in figure 3.8a was manufactured. Commencing on the left side roller, the ribbon passes closely over the green cutting mat, and then up around the final former as shown. The purpose of the cutting mat is to facilitate the progressive removal of excess kapton insulation. Even tension is retained through the process by suspending a mass from each axel. One irritating feature of the apparatus is the need to wind and unwind the left and right suspending wires respectively, every seventh turn. In hindsight, implementing a continuous pulley system would have been worth the additional effort. To maximise the packing ratio only the last two turns

are superglued. For the prevention of corrosion without substantially impeding the thermal conductivity, the coils were thinly coated with Cotronics Duralco 128 thermal epoxy. Coils resistances were then measured to determine which coil arrangement would give pairs of most similar resistance. Separated with three 2mm nylon nuts, the pairs were stacked and the foil ends folded together as shown in figure 3.8b. After finely sanding the ribbon surfaces to remove kapton residue they were soldered together across the top coil surface. Sections of 3mm diameter enamelled wire of approximating 100mm length were squarely cut, and then soldered centrally atop the coil contacts. To prevent corrosion of the electrical contacts, a single layer of MG Chemicals insulating varnish was locally applied.

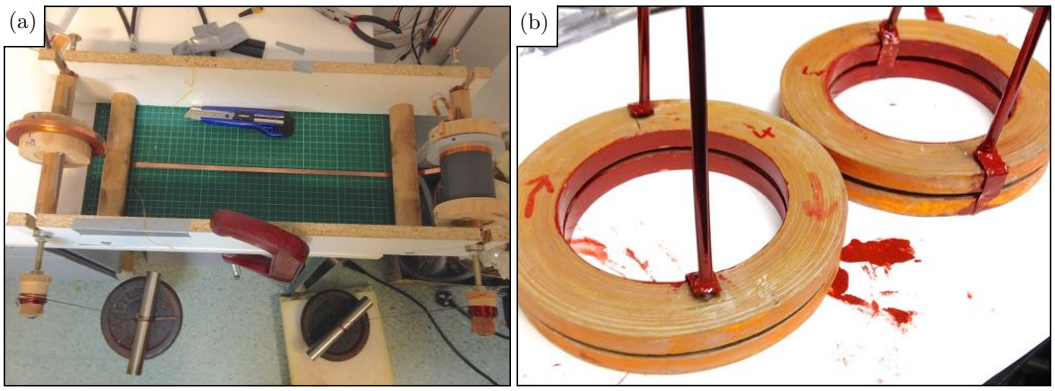

FIGURE 3.8: Quadrupole coils & winding apparatus. (a) Commencing on the left side roller the 6.35mm ribbon is passed low over the cutting mat, and then up around the final former. Before reach the otherside, excess kapton is removed against the cutting mat. To maintain tension throughout this process, a mass is hung from both axels. As the coil is wound the left weight ascends while the right descends, hence needing to be reset every seventh turn. (b) Final electrically parallel coil pairs. To prevent corrosion within the water cooling, coil were coated with Cotronics Duralco 128 thermal epoxy. Each pair is separated with three 2mm thick nylon nuts superglued to the lower coil. To prevent corrosion of the electrical contacts, a single coat of MG Chemicals insulating varnish was locally applied.

3.4.3 Mounting & Cooling

Since the four quadruple coils is expected to collectively generate 522W at the maximum anticipated ramp current of 33A, systematic cooling is required. Optical access must however be preserved. Furthermore, to avoid eddy currents during magnetic compression the water casings must be non-conductive. For mechanical stability, a rigid material with similar thermal expansion coefficient is typically chosen. *MACOR* complements most metals, including copper, for which the ratio of expansion coefficients is 0.6. For speed of production however, the present casings are acrylic, giving an expansion ratio of 0.2 (figure 3.9). For each coil pair the design essentially consists a body, providing physical support, and the lid through which currents pass. Initial tests demonstrated a flow rate of 6L/min could be mainted without detectable cavitation. This water is not wasted however, instead it recycles through the labs closed cycle sustainable water system.

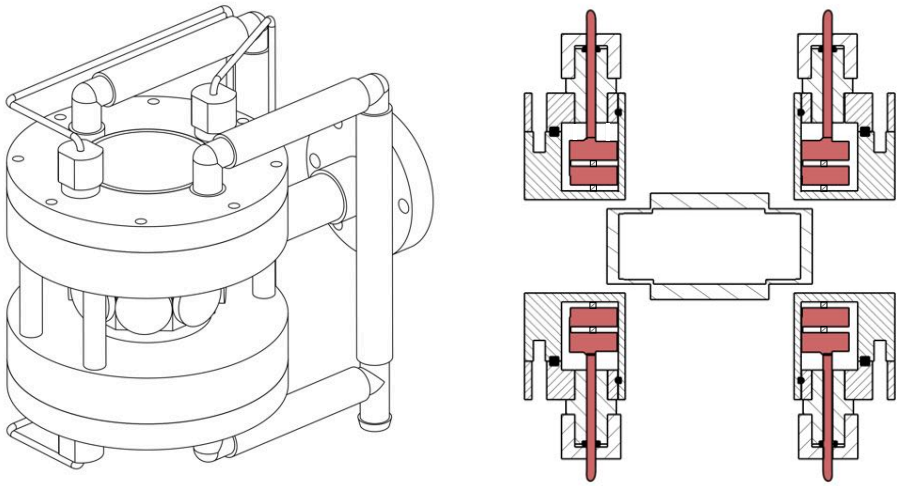

(a) (b)

FIGURE 3.9: 3D-MOT mounting and water cooling system. (a) Each quadrupole coil pair is independently encased. Satisfying the anti-helmholtz condition, the four support posts seperating the coils are 40mm long. The posts are additionally positioned to preserve optical access. While the casings in the water circuit are parallel, electrically the coils are connected through a switch box, enabling helmholtz field production by reversing the current through the upper coil pair. (b) Casing cross-section. In total 8 washers are used to seal the two lids and 4 electrical contacts. A 2mm minimum clearance is maintained about all coil surfaces bar the inner supporting surface.

3.4.4 Field Characterisation

Prior to the installation of the assembled quadrupole coils, the radial field gradient was measured for comparison with the design in figure 3.7. For a representative test the final configuration, including the water cooling system, was assembled on a spare breadboard (figure 3.10a). For spatially precise field measure a Honeywell SS94A1F hall probe was mounted from a micrometer translation stage. To increase the relative certainty of field measurements, the maximum output of a 3A supply was used. During this procedure the maximum stable $\sim$ 6L/min water flow rate was additionally used. To easily align the probe translation path with the trap centre, the zero field measurement offset was firstly noted. If the location of the trap centre corresponding to this field amplitude changed for the reverse current, this indicated the path was not radial. Hence progressively perturbing the translation stage, both vertically and rotationally, the probe path may be suitably aligned. To rigorously confirm the radial path alignment, field gradient data was taken for both current directions (figure 3.10b). Not only where both determined gradients consist with the theoretical value $b = 2.41$ G/cm/A, but the regression intersection additional confirmed the measurement path was suitably radial.

3.4.5 Optical Translation Stage

Through the larger science cell windows three optical systems compete for access. While the ODT beams are suitably detuned from the cooling light to permit the use of dichroic mirrors,

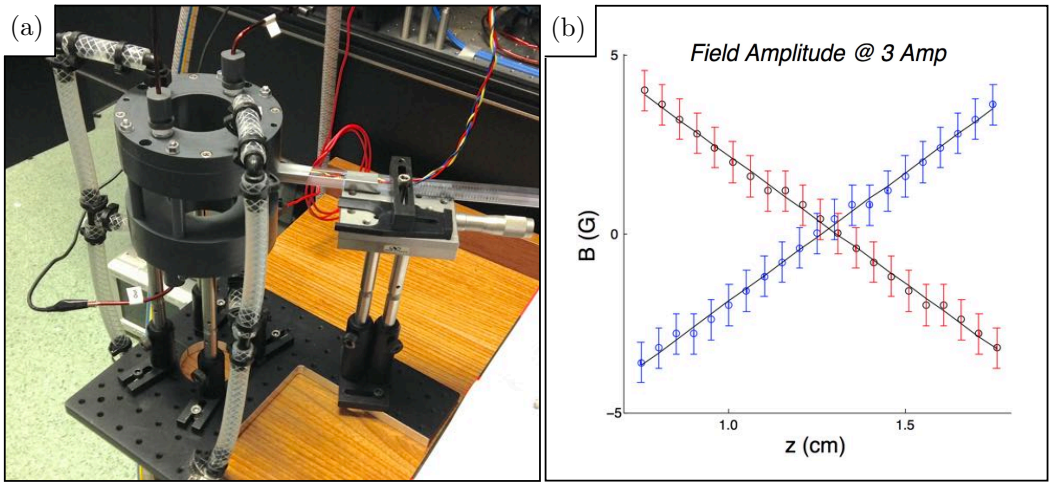

FIGURE 3.10: 3D-MOT experimental field characterisation. (a) Mounted on a micrometer translation stage with a rigid plastic rod, a Honeywell SS94A1F hall probe was used to measure the field amplitude. Since ±3A currents were used during this process to minimise the relative significance of environmental fields, the cooling system was simultaneously assembled and tested. A maximum flow rate of 6 L/min was measured with no apparent cavitation. (b) To ensure the data corresponded to a radial path through the trap centre, data was taken for both current directions. Using the recursive algorithm of [94], the field gradients $b_+ = 2.39 \pm 0.14$ G/cm/A and $b_- = 2.37 \pm 0.14$ G/cm/A were determined. Hence both are consistent with the design value $b = 2.41$ G/cm/A. Furthermore, the regression intersection field magnitude $B_0 = 0.2 \pm 2.8$ G indicates the data corresponds to a path through trap centre.

an initial challenge was to determine a method for distinguishing the vertical MOT beams from the imaging light. To prevent imaging aberration through additional optical elements, mechanical methods were proposed to remove MOT optics from the fixed imaging path, following magnetic transfer. A trivial consequence of this design is diagnostic images of the MOT must be taken through a side window. In the first incarnation only the vertical beams were linearly translatable, while the horizontal beams were rigidly mounted on the flanking breadboards. Mounted horizontally, the z-beams were each reflected through the cell using right angle prism mirrors, a feature preserved in the final design (figure 3.11). Originally the actuator was mounted beneath the left board, and the MOT collimators supported entirely by the actuator shaft. After discovering the shaft rotated however, additional guides were required, introducing frictional hysteresis. Coupled with the additional desire to free side windows for crossed ODT, the system was redesigned. Mounting the optics on a single rigid stage furthermore better preserves the relative beam alignment. Since the 100mm MOT collimators could not pass between the ODT and Bias coils (section 3.5.1), reflected input of horizontal cooling beams was required. For automated control of the linear actuator within a mechanically defined operating range, the control circuit in figure A.2 was constructed. While originally a second switch set the retracted position, the default position was instead used in the final design.

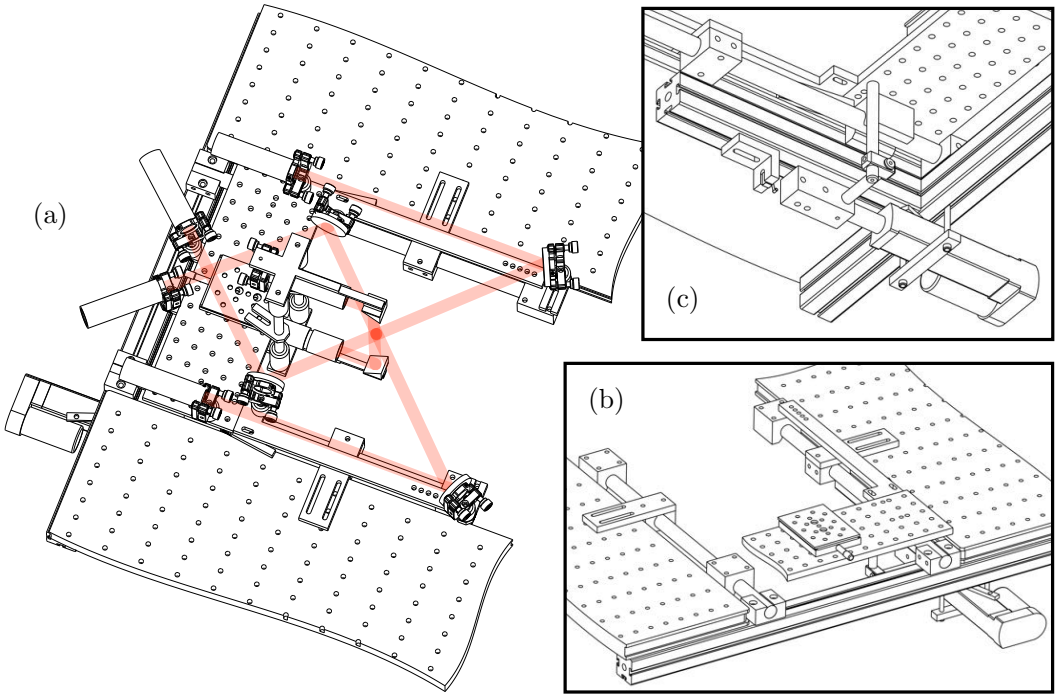

FIGURE 3.11: Actuator driven MOT translation stage. (a) To clear all science cell windows for later stage ODT confinement, the 3D-MOT optics are together mounted on a computer controlled translation stage. Outward spatial constraints imposed by the dipole optics, and inward constraints imposed by bias coils discussed in section 3.5, motivated reflected input of all four horizontal cooling beams. Similar reasoning motivated the reflected input of vertical cooling beams, which block access to the larger windows intended for imaging & scanned ODT. (b) Bare cutaway translation stage. On two rails the main board and two mirror arms are together supported by four low friction cars. For fine independent control of the vertical beam alignment a micrometer translation stage was used. (c) Attached to the board underside, a 12V Ozwerx linear actuator was used to move the stage. Automated control was facilitated using the relay control circuit in figure A.2. To set the outward stopping position a single bracket mounted switch was placed ahead of the drive rod. This location prevents torque on the stage and provides a mechanical protection against electrical circuit failure. Of the 100mm actuator range the present design uses 85mm.

3.5 Magnetic Confinement

3.5.1 Coil Design

Efficient transfer between MOT and magnetic potentials requires the close alignment of magnetic and optical scattering force centres. Helmholtz configured Bias coils are consequently required to cancel earths field, and for correcting minor physical misalignment. While both tasks could be performed with the same coil, for some applications individual addressability could be favourable. To correct fields with arbitrary direction, bias coils are required for each spatial axis. Furthermore, for driven evaporative cooling smaller impedance matched coils are required. For the present work two independent coil sets were designed (figure 3.12).

For the larger set, each coil represents a pack of three, facilitating earth field cancelation, trap alignment and broader future capacity with individual addressability. The smaller cell mounted set conversely consists just two coils per pack. With different turn number, these coils are included to provide an alternative resonant frequency for alternative magnetic trapping potentials. Treatment of these potentials is however outside the scope of this thesis. The number of turns for each coil is summarised in table B.1.

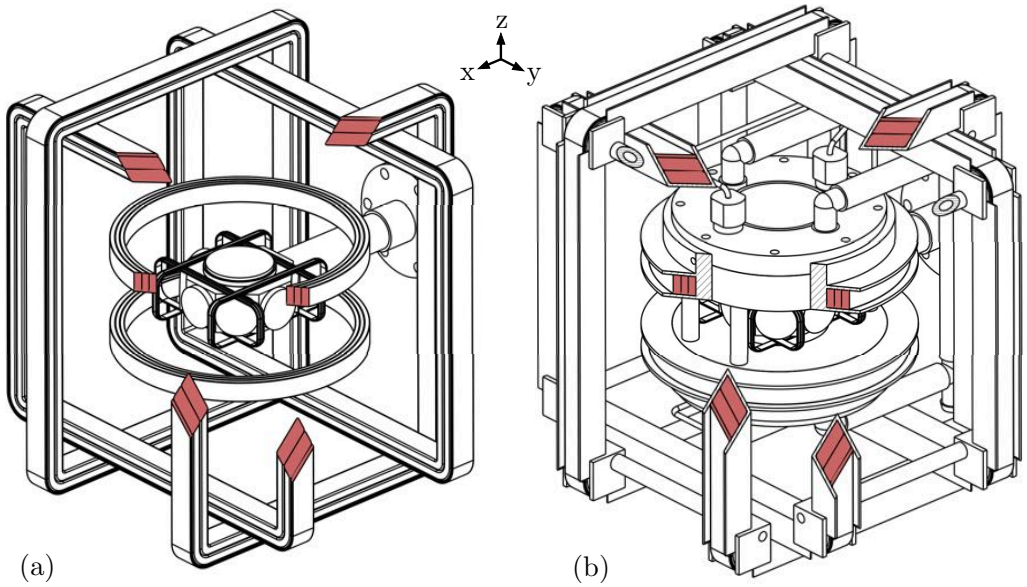

Figure 3.12: Magnetic bias and radio-frequency coil configurations. (a) exposed view illustrating the number, size and relative position of two distinct coil systems. The largest three coil pairs are in the present thesis called the bias coils, while the three pairs in direct contact with the science cell are called the rf-coils. Each bias coil pair is wound in three parts, facilitating the individual addressability of three distinct operations. This feature has greater significance when mixing AC and DC currents, as required for many magnetic potentials outside the scope of this thesis. While the first two z-bias coils were wound using 0.73mm diameter enamelled copper wire, all other bias coils were later wound with the thicker gauge 1.08mm diameter. Conversely the rf-coils are each wound in two parts using 0.45mm diameter enamelled wire. The number of turns used for each coil is summarised in table B.1. (b) mounted coil configuration which importantly maintains optical access to all science cell windows.

3.5.2 Field Characterisation

Since the bias coils are to be connected in the Helmholtz configuration, only the central field amplitude but not gradient is significant. Furthermore, the broad uniform central region greatly simplifies the measurement procedure. For each of the Bias coils a single measurement of the central field was recorded for comparison with the Radia model data (table B.2). Notice that data was taken for both single coils and coil pairs run in series. The consistency of this data indicates for mostly than no electrical shorting exists and that

coils have been reasonably manufactured as designed. Model data is additionally provided for the rf-coil fields, however no experimental data was recorded (table B.3).

3.6 Absorption Imaging

Absorption Imaging exploits the atomic clouds absorption of a resonant probe beam to form a negative image on a CCD camera or planar detector. The principle of this imaging technique is represented in the figure 3.13. Absorbing the laser light, the attenuated probe beam intensity along x will given by the *Lambert-Beer* law, where $n(y,z)$ is the density profile of atoms in the sample, I is the intensity along x and σ_0 is the scattering cross section of the probe light.

$$\frac{dI}{dx} = -n(y,z)\sigma_0 I \tag{3.1}$$

For a beam of smaller intensity than the saturation intensity of the absorption transition, the transmitted light profile will have the form $I(x,y)$ where $\bar{n}$ is the integrated intensity along the propagation x-axis, also called the column density.

$$I(y,z) = I_0(y,z)\exp\left(-\bar{n}\sigma_0\right) \tag{3.2}$$

In essence, despite its simplicity absorption imaging gives a complete snapshot of the thermodynamics of the atom cloud. The amount of light absorbed corresponds to the number of atoms in the cloud, and the spatial profile of the absorbed light corresponds to the spatial distribution and hence temperature of the atom cloud. It has one drawback in that it is an inherently destructive process for the atom cloud when using resonant or near resonant probe light, as the absorption beam heats the atom cloud through photon scattering. In practice, three images are taken in series. The first is the absorption image of the atom cloud. This is followed by a second reference image of the equal intensity probe beam without atoms. Finally, in third image the probe light extinguished to measure the non-resonant background light on the camera. For our absorption imaging, we make use of light resonant with the $(f = 2, f' = 3)$ cooling transition. Letting η represent a two dimensional digital image array, the transmission of the cloud $\bar{T}$ may be determined computationally.

$$\bar{T} = \frac{\eta_{\text{atom}} - \eta_{\text{background}}}{\eta_{\text{reference}} - \eta_{\text{background}}} \tag{3.3}$$

The atom number can then be determined integrating over the column density $\bar{n} = -\frac{\ln \bar{T}}{\sigma_0}$, with w^2 the area of single pixel of size w on the CCD detector.

$$N_{atoms} = -\frac{w^2}{\sigma_0}\sum \ln \bar{T} \tag{3.4}$$

The temperature of the atoms can be determined by measuring the spatial profile after releasing the atoms from the trapping potential, and allowing them to ballistically expand. For atoms expanding from a harmonic trap, the Gaussian width $w(t)$ of the atomic cloud grows as a function of time t.

$$w(t)^2 = {w_0}^2 + \frac{2k_B T_{th}}{m}t^2 \tag{3.5}$$

Here w_0 is the initial Gaussian width of the trapped cloud, k_B is Boltzmann's constant, m mass, and T_{th} the thermal temperature of the cloud. The imaging objective is a single f=150mm lens, placed in the $2f$ configuration, with a magnification of 1. The pixel size of the CCD camera is 6.45μm.

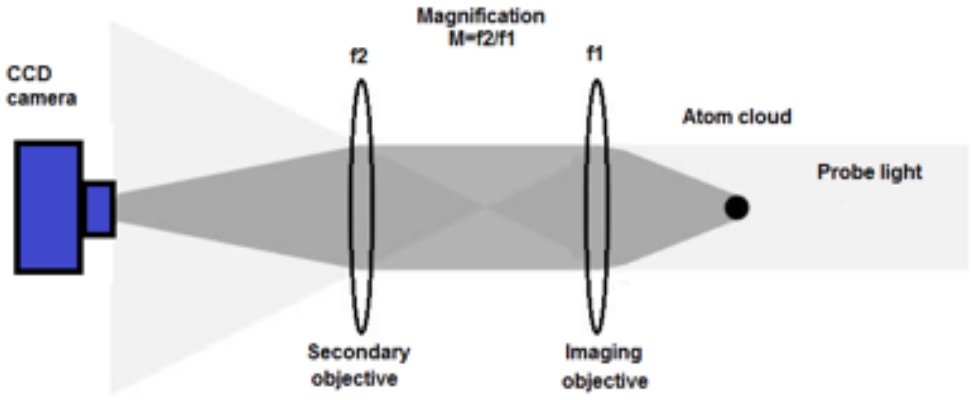

Figure 3.13: Absorption imaging operational schematic (adapted from [12]). Part of the resonant probe beam incident on the atom cloud is scattered through absorption and spontaneous emission. The shadow represented in darker grey is then focussed onto the CCD detection surface.

4

Towards Condensate Production

4.1 2D-MOT Optimisation

Coil Currents The coils are controlled by three separate current supplies, for vertical control in one coil, horizontal control in another, and the remaining two connected in series setting the field gradient. Operated with $\sim$ 5A per coil the corresponding gradient is $\sim$ 20G/cm, a value found to give the best loading conditions. This is tightly confining in the radial directions of the 2DMOT, yielding the high density beam needed to optimise flux through the 1.2 mm aperture. However, flux is observed for all currents greater than 1.5A. The optimised coil currents vary slightly, accounting for different winding efficiency and slight mechanical misalignment about glass cell and copper aperture. Additionally summarised in table B.4, the optimised vertical, horizontal and gradient currents are respectively 5.4A, 5.2A and 4.6A.

Cooling Beams Optimisation of the observed loading rate into the 3DMOT was used to optimise the 2DMOT conditions. This was achieved by pulsing on/off the 3DMOT trapping coils with a square wave of 5 second period, and observing the 3DMOT fluorescence imaged onto a CCD camera (ProSilica EC1380) whilst varying the 2DMOT optical alignment, field, and Rubidium vapour pressure. The mechanical alignment of the 2DMOT optics, beam power and the currents in the coils were first optimised to give the optimum loading. The atom flux and 3DMOT atom number was found to be greatly enhanced with the addition of the push beam, consistent with effect observed in [86, 95]. The push beam is controlled via a double passed AOM to allow the detuning and optical power to be optimised. A detuning of -20 MHz and push beam power of 300 uW, in a 5 mm beam was found to give the optimal loading. The alignment of the push beam was found to be quite critical in achieving high flux. Finally, the vapour pressure in the 2DMOT cell was varied by pulsing the Rb dispenser with various currents (up to 6 A) and periods (up to 2 mins). The best loading

conditions were observed when significant fluorescence was observed in the 2DMOT cell. The true vapour pressure in the cell trapping region during loading has yet to be measured, but can be done by measuring absorption of a resonant probe beam. However, the optimum conditions corresponded to pressure of $4 \times 10^{-}9$ bar as measured by the ion pump. The true vapour pressure of Rb in the trap region is likely to be $\sim 1 \times 10^{-}7$mbar, consistent with optimum vapour pressures seen by other groups [22].

Vacuum It is of interest to note that when the 2DMOT coils are off but 2DMOT beams left on, there is still loading into the 3DMOT, which results from the optical molasses of atoms from the 2DMOT beams. However, at normal operating pressure when the 2DMOT beams are off, there is almost no loading of atoms into the 3DMOT, indicating that the copper differential pumping aperture is performing as expected, maintaining a pressure differential of 1000 between the two cells, and velocity selecting only those atoms with small enough transverse velocities to make it through the tube, which is a negligible fraction without laser cooling from the 2DMOT beams. Thus, the 3DMOT and magnetic trap can operate with extremely long lifetimes without collisional loss or heating from stray atoms streaming from the 2DMOT cell.

4.2 3D-MOT Optimisation

Beam Alignment The beam powers were balanced by adjustments of the half-wave plates on the distribution board in a 5 step process by first balancing the X beams, the Y beams, the Z beams, and then balance of XY and XZ. Despite slight differences in coupling efficiencies into the polarisation maintaining fibres, the beams could easily be balanced in power with $< 10\%$ variation. The repump beam was also coupled into the X2 beam to provide the 3DMOT trapping region. The 3DMOT beams were mechanically aligned with the aid of an iris which reduced the beam diameter to 5 mm. The beam reflection off the glass viewports in the 3DMOT cell could be observed with the infrared scope, and the 3DMOT beams overlapped with each other and the centre of the cell by adjustment of the collimator mounts and secondary mirrors. The vertical beam prism mirrors were mechanically aligned by sharing a common mount that could be translated using a micrometer stage. The vertical beams were aligned with the centre of the vertical viewport by means of an aperture, and fine adjustment of the micrometer stage.

Load Summary The 3DMOT coils were operated at a current of 2.5 A ($\sim$ 12.3 G/cm), and detuning of -15 MHz (-2.5 linewidths). The beam powers were balanced for $\sim$ 16 mW per beam, in a beam diameter of $\sim$ 24mm. The average flux into the 3DMOT was $\sim 200 \times 10^6$ atoms per second, with a maximum 3×10^9 atom number being reached for times > 20 seconds. Figure 4.1b below shows the loading rate for atoms into the 3DMOT.

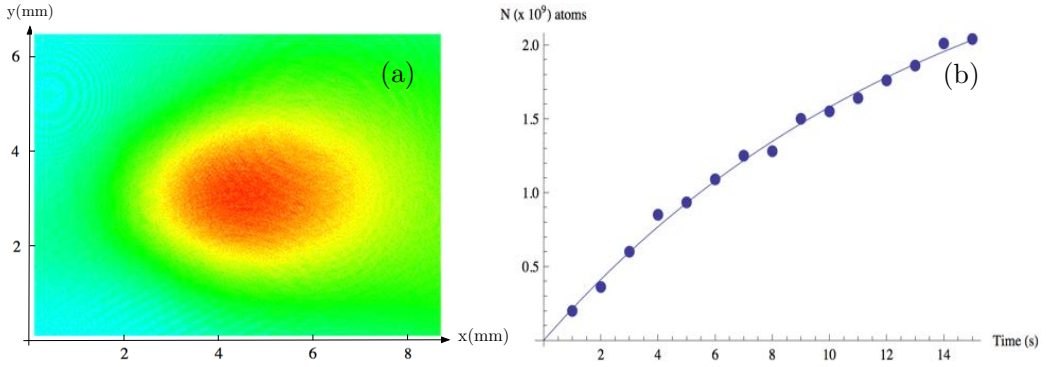

Figure 4.1: Optimised 3D-MOT load data and absorption image. (a) Absorption image of the MOT taken for a 3ms time-of-flight. (b) Load data and the numerically fit curve consistent with the model equation 2.22.

4.3 Earth Field Cancelation

The large X and Y bias coils operated in near Helmholtz condition each have 15 turns of wire for application of small bias fields, with another a set of 48 turns on the Helmholtz bias Z coils available for applying offset fields in the vertical direction to the MOT. The Earth field magnitude is on the order of ~ 0.4G, with contributions from other stray fields such as the ion pump magnets expected to contribute less than 1G in the trap region. The bias fields were calibrated, and found to give 1G/A for X&Y coils, and $\sim$ 7G/A for Z coils. To gain an indication of the necessary current required in each coil pair to cancel the stray fields, the magnetic field was first measured close to the 3DMOT cell using the Hall probe (Honeywell SS94A1F). The currents were then adjusted to roughly cancel the field component in that direction. The 3DMOT was then loaded, and the current periodically switched off in the trapping coils. When the magnetic field is imbalanced by stray fields, the MOT is preferentially pushed away in one direction, which is observed in the fluorescence of the MOT. Fine adjustment of the bias currents cancelled this effect, and were adjusted until the MOT is observed to expand uniformly when the coils are switched off. Indeed, with proper alignment, the atoms were observed to be maintained in the optical molasses from the 3DMOT beams, and persist for tens of seconds.

4.4 Compressed MOT

In order to maximise loading into the magnetic trap, we utilise a compressed MOT (CMOT) scheme, which significantly increase the density and reduces the temperature. This is achieved by detuning the cooling light while simultaneously reducing the repump light. The cooling light detuning is ramped to -150MHz (-25 linewidth) over 60ms, and the repump light is attenuated to an intensity of $\sim 40\mu\mathrm{W}/cm^2$. The magnetic trapping coils were then switched off rapidly using the switching circuit. This is followed by 1ms of optical molasses with the repump light extinguished. The repump shutter is closed and the MOT light is

allowed to continue pumping for another 3ms. With the repump light extinguished, the atoms are populated into the $f = 1$ state. The measured temperature of the atoms in the CMOT is $\sim$ 32uK, determined by measuring from absorption image of the expanding cloud when the light and coils are extinguished, and has atom number $> 1 \times 10^9$.

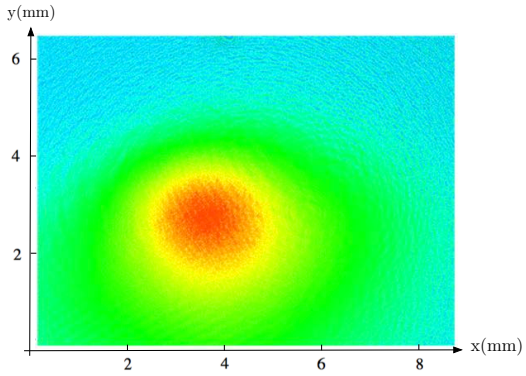

FIGURE 4.2: Magnetic trap absorption images. (a) Absorption image of $|f = 1, m_F = -1\rangle$ atoms trapped in the quadrupole trap, after 100ms. The sloshing and heating in the trap is clearly seen, indicating mode mismatch in the positions of the CMOT and the magnetic trap. (b) Absorption image of atoms released from magnetic trap at 200G/cm, held for 30 seconds in the trap, and after 3ms time of flight. The temperature of the cloud is $\sim 410\mu$K.

4.5 Magnetic Field Response

A critical component for loading effectively from the CMOT into the magnetic trap is the response time of the trapping coils when switched on. This is so that the centre of the magnetic trap can catch the atoms before they fall too far under gravity, or expand too fast from their thermal temperature. The switching circuit, in series with the coils and the current supply, employs *Insulated Gate Bi-polar Transistors* (IGBTs) to switch on and off the current to the coils. The circuit is controlled via a TTL pulse from the computer control. A bank of Zener diodes in parallel with the IGBT source to drain clamp the voltage at 500V when the gate voltage is set to zero, and allow the current to be rapidly switch off. The current switching was monitored on an oscilliscope with a clamp style current probe (HEMA model PR 430), with output signal of 10mV/A

Switch On The switch on time of the coils to rise from $0 \rightarrow 12$A, which corresponds to 60G/cm, was measured to be $\sim$ 5ms (figure 4.3a). The rise time is limited by the inductance of the coils, as well as the programming speed of the power supply. Nevertheless, in 5ms the atom cloud will only fall 122μm, which should allow relatively good transfer between the CMOT and the magnetic trap.

Switch Off Figure 4.3b below shows the switch off response of the switching circuit, with a current of 12A decaying in 44μs. The fall time is much faster than the rise time, due to the

presence of the Zener diodes in parallel with the IGBTs that clamp the voltage, and allow the current to quickly decay.

Figure 4.3: Magnetic quadrupole coil field response time. (a) The top trace is the current in the coils, with scale 10 mV/A. The rise time is $\sim$ 5ms. The bottom trace shows the rising trigger pulse for the switching circuit. (b) The top trace is the current in the coils, with scale 10mV/A. The fall time is $\sim 44\mu$s. The bottom trace shows the falling trigger pulse for the switching circuit.

4.6 Magnetic Trapping

Trap Loading The magnetic trap was loaded by programming the current to 12A, corresponding to a gradient of 60G/cm. The switch circuit was then opened to allow the current to flow. This gradient was found to give the best transfer of atoms. Figure 4.4a below shows the absorption image of the cloud 100ms after the magnetic trap was switched on. The asymmetries that can be observed in the cloud profile are from sloshing of the atoms in the trap, indicating a mismatch in the horizontal and vertical position of the magnetic trap centre relative to the CMOT centre. This is unsurprising as the MOT position is independent of gravity, whereas the magnetic trap suffers from gravitational sag, with the trap minimum some distance below the MOT centre. The maximum atom number observed transferred into the magnetic trap was $\sim 300 \times 10^6$. This is lower than hoped, but is consistent with the 33% fraction of atoms that can be trapped, as only atoms in the $|f = 1, m_F = -1\rangle$ state will be transferred. This could be improved by the application of a short optical pumping pulse with the appropriate circular polarisation, after the CMOT and prior to the magnetic trap. The mode mismatch can be solved by shifting the magnetic field zero with the additional external bias coils in the Z direction.

Trap Compression The magnetic coils were ramped held at 60G/cm for 1 second, and then ramped to a final value of 200G/cm (at 40A) over 3 seconds. The trap was then held for varying period of time and then switched off and absorption image taken. As can be seen in figure 4.4b, for a short 3ms time of flight, the cloud occupies the same 2:1 profile of the quadrupole trap, with the trap being twice as tight in the vertical direction as the horizontal

(radial) direction. The cloud temperature corresponds to 410μK, which is a factor of 2 larger than anticipated, but explained by the additional heating form the mode mismatch in the initial trap. The atoms were held in the trap for periods up to 60 seconds, with no significant loss in atom number, and no significant observation in heating. In fact, in some images, the atom number was higher after 60 seconds than after short periods. This variation is from shot to shot variation in the transfer efficiency into the trap, and variation in the MOT atom number with time. The low loss in atom number from the trap indicates the cell maintains an excellent vacuum, and is decoupled from influence of the higher pressure 2DMOT cell.

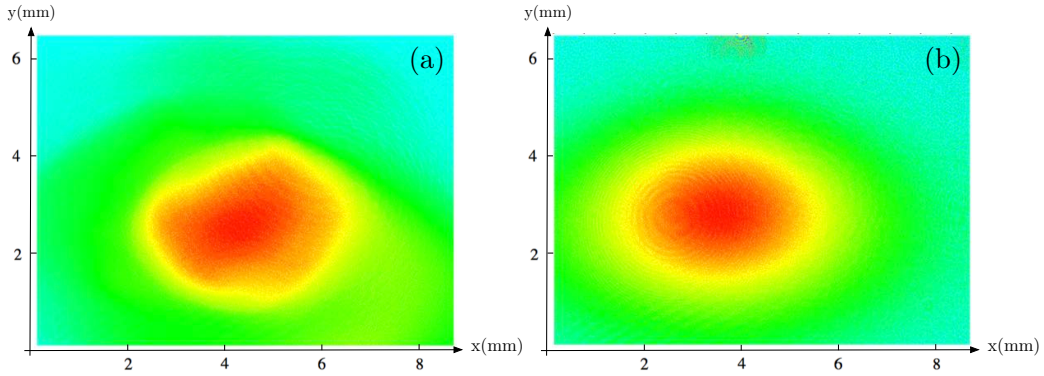

FIGURE 4.4: Magnetic trap absorption images. (a) Absorption image of $|f = 1, m_F = -1\rangle$ atoms trapped in the quadrupole trap, after 100ms. The sloshing and heating in the trap is clearly seen, indicating mode mismatch in the positions of the CMOT and the magnetic trap. (b) Absorption image of atoms released from magnetic trap at 200G/cm, held for 30 seconds in the trap, and after 3ms time of flight. The temperature of the cloud is $\sim 410\mu$K.

5 Conclusion

We have successfully generated large MOT with up to 3×10^9 atoms, and CMOT of 1.2×10^9 at temperatures of 32μK. Furthermore, long lived magnetic traps with up to 3×10^8 atoms have been formed. The transfer into the magnetic trap is however not yet optimised, and problems with the mismatch in position of the CMOT and the magnetic trap remain. These can be solved with the application of bias fields to correct for the position of the CMOT relative the magnetic trap. In addition, only $\sim$33% of the atoms in the CMOT are being transferred into the magnetic trap. This fraction could be improved by the application of circularly polarised optical pumping light prior to the magnetic trap being switched on, using light resonant with the $(f = 2 \rightarrow f' = 2)$ transition, which would preferentially decay into the $|f = 1, m_F = -1\rangle$ state. Next in the sequence is to drive evaporative cooling within the compressed magnetic trap using rf-fields. For this task an SRS DS345 frequency generator would be used. It remains then to overlap the optical dipole trap and evaporate therein to BEC. While not thoroughly treated in the present thesis, many preliminary steps toward dipole trapping, including beams waist characterisations, have been completed. Consequently, the remaining two stages between the present achievement and the production of BEC are expected to proceed more rapidly. As originally outlined (figure 1.1), the foremost intension is to pursue all-optical *Time Averaged Adiabatic Potentials* (TAAP). For Sagnac atom interferometry in particular, two dimensional scanned ODT configurations are of principle interest.

A
Optical Shutter Design

Since the frequency of each beam is finely tuned with an AOM on the laser table, high speed shutters on the distribution board are not required. Instead the AOM response time is sufficient for rapid switching. A simple and cheap shutter design was therefore implemented. This design consists an Omron SPDT electrical relay with a narrow retractable stanley knife blade affixed on top (figure A.1). For strength a short blade section is soldered to the relay while the remaining longer section was super glued at the appropriate angle in situ. For fine positional adjustment the relay itself was glued atop a regular optical base. As represented in figure 3.4, five such shutters were made, requiring a multi-port computing control box. The implemented circuit is represented in figure A.2.

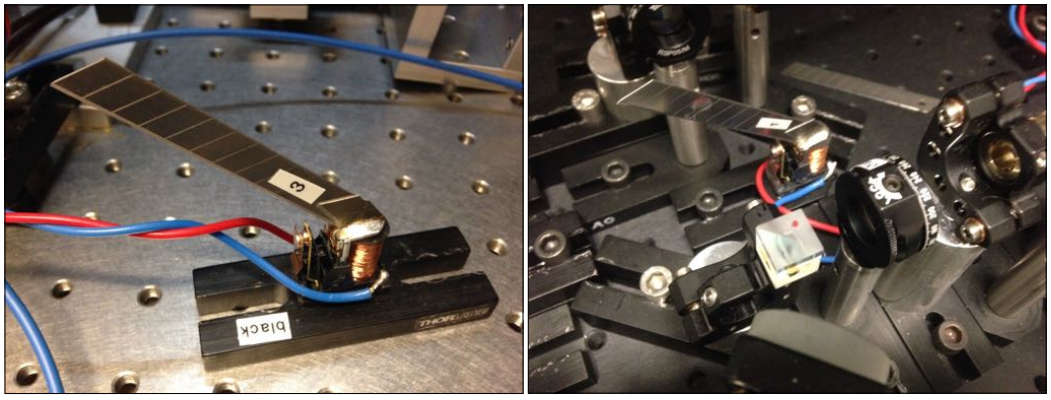

FIGURE A.1: Simple optical shutter design, consisting an Omron SPDT electrical relay with a generic narrow stanley knife blade affixed on top. For strength a short blade section is soldered to the relay while the remaining longer section was super glued at the appropriate angle in situ. For fine positional adjustment the relay itself was glued atop a regular optical base.

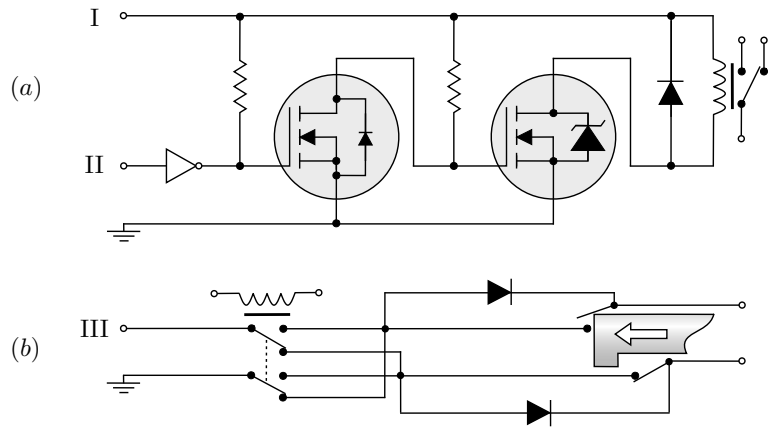

FIGURE A.2: Electrical relay and linear actuator computer control circuit [96]. (a) Electrical relay control circuit used foremostly to control four self-made shutters. This circuit additionally controls the second linear actuator circuit. The components in this circuit are: ULN2003A Darlington Array Chip, 2N7000 FET, HUF75639P MOSFET, 1N5404 Rectifier and two 10 kΩ resisters. (b) Linear actuator control circuit providing a method for limiting the range of motion. In the represented configuration the actuator rod is driven left until opening the appropriate switch. While this breaks the forward drive circuit, the parallel diode enables the reverse motion until the second switch is opened. (I) 5V for the Omron relays as manufactured. The shutter relays however require 9V to move the additional weight of blades soldered atop. (II) TTL coaxial input. (III) 12V Ozwerx linear actuator drive voltage.

B
Data Tables

Table B.1: Magnetic coil turn number summary.

Type	Axis	Layer	Turns
Bias	X	1	60
		2	60
		3	15
	Y	1	60
		2	60
		3	15
	Z	1	48
		2	48
		3	56
RF	X	1	24
		2	5
	Y	1	24
		2	5
	Z	1	2
		2	13
MOT	2D	-	40
	3D	-	90

TABLE B.2: Experimental bias coil field amplitudes.

Axis	Pack	Coil	Radia (G)	Measured (G)
		a	2.27	2.28 ± 0.06
	1	b†	2.23	2.36 ± 0.06
		c	0.55	0.54 ± 0.04
		a	2.27	2.16 ± 0.06
X	2	b	2.23	2.12 ± 0.06
		c	0.55	0.54 ± 0.04
		a	4.55	4.5 ± 0.1
	1∧2	b	4.46	4.5 ± 0.1
		c	1.10	1.10 ± 0.05
		a	2.27	2.10 ± 0.06
	1	b	2.23	2.10 ± 0.06
		c	0.55	0.52 ± 0.02
		a	2.27	2.18 ± 0.06
Y	2	b	2.23	2.28 ± 0.06
		c	0.55	0.52 ± 0.04
		a	4.55	4.4 ± 0.1
	1∧2	b	4.46	4.5 ± 0.1
		c	1.10	1.04 ± 0.05
		a	3.73	3.40 ± 0.08
	1	b	3.63	3.34 ± 0.08
		c	4.11	3.78 ± 0.08
		a	3.73	3.60 ± 0.08
Z	2	b	3.63	3.56 ± 0.08
		c	4.12	3.96 ± 0.08
		a	7.46	7.0 ± 0.2
	1∧2	b	7.26	6.9 ± 0.1
		c	8.23	7.7 ± 0.2

TABLE B.3: Theoretical rf-coil field amplitudes.

Axis	Pack	Coil	Radia (G)
X	1∨2	a	1.96
		b	0.416
	1∧2	a	3.92
		b	0.832
Y	1∨2	a	1.86
		b	0.396
	1∧2	a	3.72
		b	0.793
Z	1∨2	a	0.336
		b	2.18
	1∧2	a	0.672
		b	4.37

TABLE B.4: Optimised 2D-MOT parameters.

Currents	Vertical	5.4A
	Horizontal	5.2A
	Gradient	4.6A
Push Beam	Power	300μW
	Diameter	5mm
	Detuning	-20MHz
Cooling Beams	Power/Beam	40mW
	Detuning	-15MHz

TABLE B.5: Optimised 3D-MOT parameters.

Magnetic Coils	Current	2.5A
	Power	3.0W
	Gradient	12.3G/cm
Cooling Beams	Power/Beam	16mW
	Diameter	24mm
	Detuning	-15MHz
Loading	Max Number	3×10^9
	Time	> 20s
	Mean Rate	2×10^8 /s

References

[1] C. Chin, R. Grimm, P. Julienne, and E. Tiesinga. *Feshbach resonances in ultracold gases*. Rev. Mod. Phys. (2010).

[2] A. Görlitz, T. L. Gustavson, A. E. Leanhardt, R. Löw, A. P. Chikkatur, S. Gupta, S. Inouye, D. E. Pritchard, and W. Ketterle. *Sodium bose-einstein condensates in the f=2 state in a large-volume optical trap*. Phys. Rev. Lett. **90**, 090401 (2003). URL `http://link.aps.org/doi/10.1103/PhysRevLett.90.090401`.

[3] S. B. Papp, J. M. Pino, R. J. Wild, S. Ronen, C. E. Wieman, D. S. Jin, and E. A. Cornell. *Bragg spectroscopy of a strongly interacting rb85 bose-einstein condensate*. Phys. Rev. Lett. **101**, 135301 (2008). URL `http://link.aps.org/doi/10.1103/PhysRevLett.101.135301`.

[4] P. T. Ernst, S. Gotze, J. S. Krauser, K. Pyka, D.-S. Luhmann, D. Pfannkuche, and K. Sengstock. *Probing superfluids in optical lattices by momentum-resolved bragg spectroscopy*. Nat Phys **6**(1), 56 (2010). URL `http://dx.doi.org/10.1038/nphys1476`.

[5] S. A. Haine and A. J. Ferris. *Surpassing the standard quantum limit in an atom interferometer with four-mode entanglement produced from four-wave mixing*. Phys. Rev. A **84**, 043624 (2011). URL `http://link.aps.org/doi/10.1103/PhysRevA.84.043624`.

[6] D. Comparat, A. Fioretti, G. Stern, E. Dimova, B. L. Tolra, and P. Pillet. *Optimized production of large bose-einstein condensates*. Phys. Rev. A **73**, 043410 (2006). URL `http://link.aps.org/doi/10.1103/PhysRevA.73.043410`.

[7] Y.-J. Lin, A. R. Perry, R. L. Compton, I. B. Spielman, and J. V. Porto. *Rapid production of 87rb bose-einstein condensates in a combined magnetic and optical potential*. Physical Review A (2009).

[8] E. L. Raab, M. Prentiss, A. Cable, S. Chu, and D. E. Pritchard. *Trapping of neutral sodium atoms with radiation pressure*. Phys. Rev. Lett. **59**, 2631 (1987). URL `http://link.aps.org/doi/10.1103/PhysRevLett.59.2631`.

[9] M.H.Anderson, J.R.Ensher, M.R.Matthews, C.E.Wieman, and E.A.Cornell. *Observation of bose-einstein condensation in a dilute atomic vapor*. Science (1995).

[10] K. B. Davis, M. O. Mewes, M. R. Andrews, N. J. van Druten, D. S. Durfee, D. M. Kurn, and W. Ketterle. *Bose-einstein condensation in a gas of sodium atoms*. Phys. Rev. Lett. **75**, 3969 (1995). URL `http://link.aps.org/doi/10.1103/PhysRevLett.75.3969`.

[11] M. Pappa. *Imaging Bose-Einstein Condensates at Ultra-Low Atom-Numbers and Time Averaged Adiabatic Potentials*. Ph.D. thesis, University of Crete (2011).

[12] I. L. H. Humbert. *All-optical 87Rb Bose-Einstein condensate apparatus: Construction and operation*. Ph.D. thesis, University of Queensland (2012).

[13] D. V. Schroeder. *An Introduction to Thermal Physics* (Addison Wesley Longman, 2000).

[14] W. Bao, D. Jaksch, and P. A. Markowich. *Numerical solution of the gross–pitaevskii equation for bose–einstein condensation*. Journal of Computational Physics **187**(1), 318 (2003). URL http://www.sciencedirect.com/science/article/pii/S0021999103001025.

[15] V. Bagnato, D. E. Pritchard, and D. Kleppner. *Bose-einstein condensation in an external potential*. Phys. Rev. A **35**, 4354 (1987). URL http://link.aps.org/doi/10.1103/PhysRevA.35.4354.

[16] D. J. Griffiths. *Introduction to Quantum Mechanics* (Pearson, 2005), 2nd ed.

[17] D. A. Steck. *Rubidium 87 d line data* (2003). URL http://steck.us/alkalidata.

[18] A. Corney. *Atomic and Laser Spectroscopy* (Oxford University Press, 1977).

[19] V. Balykin. *Cyclic interaction of na atoms with circularly polarized laser radiation*. Optics Communications **33**(1), 31 (1980). URL http://www.sciencedirect.com/science/article/pii/0030401880900875.

[20] J. M. Hollas. *Modern Spectroscopy* (John Wiley & Sons, Ltd, 2013), 4th ed.

[21] W. D. Phillips, J. V. Prodan, and H. J. Metcalf. *Laser cooling and electromagnetic trapping of neutral atoms*. J. Opt. Soc. Am. B **2**(11), 1751 (1985). URL http://josab.osa.org/abstract.cfm?URI=josab-2-11-1751.

[22] K. Dieckman. *Bose-Einstein Condensation with High Atom Number in a Deep Magnetic Trap*. Ph.D. thesis, Universiteit van Amsterdam (2001).

[23] J. Weiner, V. S. Bagnato, S. Zilio, and P. S. Julienne. *Experiments and theory in cold and ultracold collisions*. Rev. Mod. Phys. **71**, 1 (1999). URL http://link.aps.org/doi/10.1103/RevModPhys.71.1.

[24] R. Grimm and M. Weidemüller. *Optical dipole traps for neutral atoms*. Elsevier (2000).

[25] J. D. Miller, R. A. Cline, and D. J. Heinzen. *Photoassociation spectrum of ultracold rb atoms*. Phys. Rev. Lett. **71**, 2204 (1993). URL http://link.aps.org/doi/10.1103/PhysRevLett.71.2204.

[26] C. V. Heer. *Feasibility of containment of quantum magnetic dipoles*. Review of Scientific Instruments **34**(5) (1963). URL http://scitation.aip.org/content/aip/journal/rsi/34/5/10.1063/1.1718426.

[27] D. E. Pritchard. *Cooling neutral atoms in a magnetic trap for precision spectroscopy.* Phys. Rev. Lett. **51**, 1336 (1983). URL http://link.aps.org/doi/10.1103/PhysRevLett.51.1336.

[28] A. L. Migdall, J. V. Prodan, W. D. Phillips, T. H. Bergeman, and H. J. Metcalf. *First observation of magnetically trapped neutral atoms.* Phys. Rev. Lett. **54**, 2596 (1985). URL http://link.aps.org/doi/10.1103/PhysRevLett.54.2596.

[29] E. Tiesinga, A. J. Moerdijk, B. J. Verhaar, and H. T. C. Stoof. *Conditions for bose-einstein condensation in magnetically trapped atomic cesium.* Phys. Rev. A **46**, R1167 (1992). URL http://link.aps.org/doi/10.1103/PhysRevA.46.R1167.

[30] M.-O. Mewes, M. R. Andrews, N. J. van Druten, D. M. Kurn, D. S. Durfee, and W. Ketterle. *Bose-einstein condensation in a tightly confining dc magnetic trap.* Phys. Rev. Lett. **77**, 416 (1996). URL http://link.aps.org/doi/10.1103/PhysRevLett.77.416.

[31] P. Zeeman. *The effect of magnetisation on the nature of light emitted by a substance.* Nature **55**(1424), 347 (1897).

[32] G. Breit and I. I. Rabi. *Measurement of nuclear spin.* Phys. Rev. **38**, 2082 (1931). URL http://link.aps.org/doi/10.1103/PhysRev.38.2082.2.

[33] W. Phillips, ed. *Some problems and possibilities for quasistatic neutral particle trapping*, vol. 653. NBS (Proceedings of the Workshop on Spectroscopic Applications of Slow Atomic Beams, Gaithersburg, 1983).

[34] D. M. Brink and C. V. Sukumar. *Majorana spin-flip transitions in a magnetic trap.* Phys. Rev. A **74**, 035401 (2006). URL http://link.aps.org/doi/10.1103/PhysRevA.74.035401.

[35] E. F. Nichols and G. F. Hull. *The pressure due to radiation (second paper).* Phys. Rev. (Series I) **17**, 26 (1903). URL http://link.aps.org/doi/10.1103/PhysRevSeriesI.17.26.

[36] P. Lebedew. *The pressure of light on gasses an experimental study for the theory of comet's tails.* The Astrophysical Journal **XXXI**(5), 385 (1910).

[37] A. Einstein. *On the elctrodynamics of moving bodies.* Ann. Phys. **17**(891) (1905).

[38] L. d. Broglie. *Xxxv. a tentative theory of light quanta.* Philosophical Magazine Series 6 **47**(278), 446 (1924). URL http://www.tandfonline.com/doi/abs/10.1080/14786442408634378.

[39] H. E. IVES and G. R. STILWELL. *An experimental study of the rate of a moving atomic clock.* J. Opt. Soc. Am. **28**(7), 215 (1938). URL http://www.opticsinfobase.org/abstract.cfm?URI=josa-28-7-215.

[40] R. Schlegel. *Radiation pressure on a rapidly moving surface.* American Journal of Physics **28**(8), 687 (1960). URL http://scitation.aip.org/content/aapt/journal/ajp/28/8/10.1119/1.1935956.

[41] J. Terrell. *Radiation pressure on a relativistically moving mirror.* American Journal of Physics **29**(9), 644 (1961). URL http://scitation.aip.org/content/aapt/journal/ajp/29/9/10.1119/1.1937875.

[42] W. Rindler and D. W. Sciama. *Radiation pressure on a rapidly moving surface.* American Journal of Physics **29**(9), 643 (1961). URL http://scitation.aip.org/content/aapt/journal/ajp/29/9/10.1119/1.1937874.

[43] D. SAVICKAS. *Dynamical effects of isotropic radiation on spherical particles.* J. Opt. Soc. Am. **60**(9), 1240 (1970). URL http://www.opticsinfobase.org/abstract.cfm?URI=josa-60-9-1240.

[44] A. Ashkin. *Acceleration and trapping of particles by radiation pressure.* Phys. Rev. Lett. **24**, 156 (1970). URL http://link.aps.org/doi/10.1103/PhysRevLett.24.156.

[45] W.-C. Tsai and R. J. Pogorzelski. *Eigenfunction solution of the scattering of beam radiation fields by spherical objects.* J. Opt. Soc. Am. **65**(12), 1457 (1975). URL http://www.opticsinfobase.org/abstract.cfm?URI=josa-65-12-1457.

[46] A. Kazantsev. *Acceleration of atoms by a resonance field.* Sov. Phys. JETP **36**(5), 861 (1973).

[47] A. Kazantsev. *The acceleration of atoms by light.* Sov. Phys. JETP **39**(784) (1974).

[48] V. Letokhov, V. Minogin, and B. Pavlik. *Cooling and capture of atoms and molecules by a resonant light field.* Sov. Phys. JETP **45**(4), 698 (1977).

[49] V. Minogin and O. Serimaa. *Resonant light pressure forces in a strong standing laser wave.* Optics Communications **30**(3), 373 (1979). URL http://www.sciencedirect.com/science/article/pii/0030401879903742.

[50] A. Ashkin. *Trapping of atoms by resonance radiation pressure.* Phys. Rev. Lett. **40**, 729 (1978). URL http://link.aps.org/doi/10.1103/PhysRevLett.40.729.

[51] J. E. Bjorkholm, R. R. Freeman, A. Ashkin, and D. B. Pearson. *Observation of focusing of neutral atoms by the dipole forces of resonance-radiation pressure.* Phys. Rev. Lett. **41**, 1361 (1978). URL http://link.aps.org/doi/10.1103/PhysRevLett.41.1361.

[52] S. Chu, J. E. Bjorkholm, A. Ashkin, and A. Cable. *Experimental observation of optically trapped atoms.* Phys. Rev. Lett. **57**, 314 (1986). URL http://link.aps.org/doi/10.1103/PhysRevLett.57.314.

[53] J. P. Gordon and A. Ashkin. *Motion of atoms in a radiation trap.* Phys. Rev. A **21**, 1606 (1980). URL http://link.aps.org/doi/10.1103/PhysRevA.21.1606.

[54] A. Ashkin and J. P. Gordon. *Stability of radiation-pressure particle traps: an optical earnshaw theorem.* Opt. Lett. **8**(10), 511 (1983). URL http://ol.osa.org/abstract.cfm?URI=ol-8-10-511.

[55] W. T. Scott. *Who was earnshaw?* American Journal of Physics **27**(6), 418 (1959). URL http://scitation.aip.org/content/aapt/journal/ajp/27/6/10.1119/1.1934886.

[56] V. G. Minogin. *Resonance-radiation pressure on atoms in symmetrical light fields.* Opt. Lett. **10**(4), 179 (1985). URL http://ol.osa.org/abstract.cfm?URI=ol-10-4-179.

[57] A. Ashkin. *Stable radiation-pressure particle traps using alternating light beams.* Opt. Lett. **9**(10), 454 (1984). URL http://ol.osa.org/abstract.cfm?URI=ol-9-10-454.

[58] D. E. Pritchard, E. L. Raab, V. Bagnato, C. E. Wieman, and R. N. Watts. *Light traps using spontaneous forces.* Phys. Rev. Lett. **57**, 310 (1986). URL http://link.aps.org/doi/10.1103/PhysRevLett.57.310.

[59] W. D. Phillips. *Laser cooling and trapping of neutral atoms.* Rev. Mod. Phys pp. 721–741 (1998).

[60] T. Hänsch and A. Schawlow. *Cooling of gases by laser radiation.* Optics Communications **13**(1), 68 (1975). URL http://www.sciencedirect.com/science/article/pii/0030401875901595.

[61] S. Chu, L. Hollberg, J. E. Bjorkholm, A. Cable, and A. Ashkin. *Three-dimensional viscous confinement and cooling of atoms by resonance radiation pressure.* Phys. Rev. Lett. **55**, 48 (1985). URL http://link.aps.org/doi/10.1103/PhysRevLett.55.48.

[62] J. Javanainen and S. Stenholm. *Broad band resonant light pressure: Ii. cooling gases.* Applied physics **21**(2), 163 (1980). URL http://dx.doi.org/10.1007/BF00900679.

[63] J. Javanainen. *Light-pressure cooling of trapped ions in three dimensions.* Applied physics **23**(2), 175 (1980). URL http://dx.doi.org/10.1007/BF00899714.

[64] R. J. Cook. *Theory of resonance-radiation pressure.* Phys. Rev. A **22**, 1078 (1980). URL http://link.aps.org/doi/10.1103/PhysRevA.22.1078.

[65] V. G. Minogin. *Theory of a radiative atomic trap.* Soviet Journal of Quantum Electronics **12**(3), 299 (1982). URL http://stacks.iop.org/0049-1748/12/i=3/a=A09.

[66] P. D. Lett, W. D. Phillips, S. L. Rolston, C. E. Tanner, R. N. Watts, and C. I. Westbrook. *Optical molasses.* J. Opt. Soc. Am. B **6**(11), 2084 (1989). URL http://josab.osa.org/abstract.cfm?URI=josab-6-11-2084.

[67] C. Foot. *Laser cooling and trapping of atoms.* Contem. Phys. **32**(6), 369 (1991).

[68] M. Fox. *Quantum Optics An Introduction* (Oxford University Press, 2006).

[69] Y. Shevy, D. S. Weiss, P. J. Ungar, and S. Chu. *Bimodal speed distributions in laser-cooled atoms.* Phys. Rev. Lett. **62**(optical molasses), 1118 (1989). URL http://link.aps.org/doi/10.1103/PhysRevLett.62.1118.

[70] J. Dalibard and C. Cohen-Tannoudji. *Laser cooling below the doppler limit by polarization gradients: simple theoretical models.* J. Opt. Soc. Am. B **6**(11), 2023 (1989). URL http://josab.osa.org/abstract.cfm?URI=josab-6-11-2023.

[71] P. J. Ungar, D. S. Weiss, E. Riis, and S. Chu. *Optical molasses and multilevel atoms: theory.* J. Opt. Soc. Am. B **6**(11), 2058 (1989). URL http://josab.osa.org/abstract.cfm?URI=josab-6-11-2058.

[72] D. S. Weiss, E. Riis, Y. Shevy, P. J. Ungar, and S. Chu. *Optical molasses and multilevel atoms: experiment.* J. Opt. Soc. Am. B **6**(11), 2072 (1989). URL http://josab.osa.org/abstract.cfm?URI=josab-6-11-2072.

[73] Y.Castin, J.Dalibard, and C.Cohen-Tannoudli. *The limits of sisyphus cooling* (1991).

[74] T. Walker, D. Sesko, and C. Wieman. *Collective behavior of optically trapped neutral atoms.* Phys. Rev. Lett. **64**, 408 (1990). URL http://link.aps.org/doi/10.1103/PhysRevLett.64.408.

[75] B. T. Sheard. *Magnetic Transport and Bose-Einstein Condensation of Rubidium Atoms.* Ph.D. thesis, University of Oxford (2010).

[76] G. L. Gattobigio, T. Pohl, G. Labeyrie, and R. Kaiser. *Scaling laws for large magneto-optical traps.* Physica Scripta **81**(2), 025301 (2010). URL http://stacks.iop.org/1402-4896/81/i=2/a=025301.

[77] W. Petrich, M. H. Anderson, J. R. Ensher, and E. A. Cornell. *Stable, tightly confining magnetic trap for evaporative cooling of neutral atoms.* Phys. Rev. Lett. **74**, 3352 (1995). URL http://link.aps.org/doi/10.1103/PhysRevLett.74.3352.

[78] M. T. DePue, S. L. Winoto, D. Han, and D. S. Weiss. *Transient compression of a {MOT} and high intensity fluorescent imaging of optically thick clouds of atoms.* Optics Communications **180**(1–3), 73 (2000). URL http://www.sciencedirect.com/science/article/pii/S003040180000701X.

[79] W. Petrich, M. H. Anderson, J. R. Ensher, and E. A. Cornell. *Behavior of atoms in a compressed magneto-optical trap.* J. Opt. Soc. Am. B **11**(8), 1332 (1994). URL http://josab.osa.org/abstract.cfm?URI=josab-11-8-1332.

[80] W. D. Phillips and H. Metcalf. *Laser deceleration of an atomic beam.* Phys. Rev. Lett. **48**, 596 (1982). URL http://link.aps.org/doi/10.1103/PhysRevLett.48.596.

[81] S. Weyers, E. Aucouturier, C. Valentin, and N. Dimarcq. *A continuous beam of cold cesium atoms extracted from a two-dimensional magneto-optical trap.* Optics Communications **143**(1–3), 30 (1997). URL http://www.sciencedirect.com/science/article/pii/S003040189700312X.

[82] C. Adams and E. Riis. *Laser cooling and trapping of neutral atoms.* Progress in Quantum Electronics **21**(1), 1 (1997). URL http://www.sciencedirect.com/science/article/pii/S0079672796000067.

[83] L. Bennie. *Design and construction of a zeeman slower for* ^{85}Rb *and* ^{87}Rb. Monash University.

[84] Z. T. Lu, K. L. Corwin, M. J. Renn, M. H. Anderson, E. A. Cornell, and C. E. Wieman. *Low-velocity intense source of atoms from a magneto-optical trap.* Phys. Rev. Lett. **77**, 3331 (1996). URL http://link.aps.org/doi/10.1103/PhysRevLett.77.3331.

[85] J. Schoser, A. Batär, R. Löw, V. Schweikhard, A. Grabowski, Y. B. Ovchinnikov, and T. Pfau. *Intense source of cold rb atoms from a pure two-dimensional magneto-optical trap.* Phys. Rev. A **66**, 023410 (2002). URL http://link.aps.org/doi/10.1103/PhysRevA.66.023410.

[86] S. Chaudhuri, S. Roy, and C. Unnikrishnan. *Realization of an intense cold rb atomic beam based on a two-dimensional magneto-optical trap: Experiments and comparison with simulations.* Physical Review A (2006).

[87] J. Plewa, E. Tanner, D. Mueth, and D. Grier. *Processing carbon nanotubes with holographic optical tweezers.* Opt. Express **12**(9), 1978 (2004). URL http://www.opticsexpress.org/abstract.cfm?URI=oe-12-9-1978.

[88] M. Dao, C. Lim, and S. Suresh. *Mechanics of the human red blood cell deformed by optical tweezers.* Journal of the Mechanics and Physics of Solids **51**(11–12), 2259 (2003). Proceedings of a Symposium on Dynamic Failure and Thin Film Mechanics, honoring Professor L.B. Freund, URL http://www.sciencedirect.com/science/article/pii/S0022509603001595.

[89] R. W. Schmieder, A. Lurio, and W. Happer. *Quadratic stark effect in the* $^2p_{\frac{3}{2}}$ *states of the alkali atoms.* Phys. Rev. A **3**, 1209 (1971). URL http://link.aps.org/doi/10.1103/PhysRevA.3.1209.

[90] A. Khadjavi, A. Lurio, and W. Happer. *Stark effect in the excited states of rb, cs, cd, and hg.* Phys. Rev. **167**, 128 (1968). URL http://link.aps.org/doi/10.1103/PhysRev.167.128.

[91] C. S. Adams, H. J. Lee, N. Davidson, M. Kasevich, and S. Chu. *Evaporative cooling in a crossed dipole trap.* Phys. Rev. Lett. **74**, 3577 (1995). URL http://link.aps.org/doi/10.1103/PhysRevLett.74.3577.

[92] S. K. Schnelle, E. D. van Ooijen, M. J. Davis, N. R. Heckenberg, and H. Rubinsztein-Dunlop. *Versatile two-dimensional potentials for ultra-cold atoms.* Opt. Express **16**(3), 1405 (2008). URL http://www.opticsexpress.org/abstract.cfm?URI=oe-16-3-1405.

[93] E. A. Donley, T. P. Heavner, F. Levi, M. O. Tataw, and S. R. Jefferts. *Double-pass acousto-optic modulator system.* Review of Scientific Instruments **76**(6), 063112 (2005). URL http://scitation.aip.org/content/aip/journal/rsi/76/6/10.1063/1.1930095.

[94] D. York, N. M. Evensen, M. L. Martnez, and J. De Basabe Delgado. *Unified equations for the slope, intercept, and standard errors of the best straight line.* American Journal of Physics **72**(3), 367 (2004). URL http://scitation.aip.org/content/aapt/journal/ajp/72/3/10.1119/1.1632486.

[95] T. Uehlinger. *A 2D Magneto-Optical Trap as a High-Flux Source of Cold Potassium Atoms.* Master's thesis, Swiss Federal Institute of Technology Zurich (2008).

[96] A. Stummer. *Research lab technology.* Electronic Archive (2014). URL http://www.physics.utoronto.ca/ astummer/pub/mirror/Projects/index.html.